Rep. Prog. Phys. **62** (1999) 809–858. Printed in the UK PII: S0034-4885(99)79146-3

The correlation between mechanical stress and magnetic anisotropy in ultrathin films

D Sander†
Max-Planck-Institut für Mikrostrukturphysik, Weinberg 2, D-06120 Halle, Germany

Received 29 December 1998

Abstract

The impact of stress-driven structural transitions and of film strain on the magnetic properties of nm ferromagnetic films is discussed. The stress-induced bending of film–substrate composites is analysed to derive information on film stress due to lattice mismatch or due to surface-stress effects. The magneto–elastic coupling in epitaxial films is determined *directly* from the magnetostrictive bending of the substrate. The combination of stress measurements with magnetic investigations by the magneto-optical Kerr effect (MOKE) reveals the modification of the magnetic anisotropy by film stress. Stress–strain relations are derived for various epitaxial orientations to facilitate the analysis of the substrate curvature. Biaxial film stress and magneto–elastic coupling coefficients are measured in epitaxial Fe films *in situ* on W single-crystal substrates. Tremendous film stress of more than 10 GPa is measured in pseudomorphic Fe layers, and the important role of film stress as a driving force for the formation of misfit distortions and for inducing changes of the growth mode in monolayer thin films is presented. The direct measurement of the magneto–elastic coupling in epitaxial films proves that the magnitude and sign of the magneto–elastic coupling deviate from the respective bulk value. Even a small film strain of order 0.1% is found to induce a significant change of the effective magneto–elastic coupling coefficient. This peculiar behaviour is ascribed to a second-order strain dependence of the magneto–elastic energy density, in contrast to the linear strain dependence that is valid for bulk samples.

† E-mail address: sander@mpi-halle.de

0034-4885/99/050809+50$59.50

Contents

1. Introduction

The important role of mechanical stress on magnetic anisotropy is well known from experiments on the effect of externally applied stress on the magnetism of *bulk* samples [1–4]. The goal of this review is to elucidate the correlation between mechanical stress and magnetic properties of ultrathin films. Recent experiments indicated that the role of epitaxial misfit between film and substrate material for film stress and magneto–elastic properties cannot be simply extrapolated from the respective bulk behaviour. Some authors introduced surface magneto–elastic coupling coefficients to account for the novel magneto–elastic properties. Sun and O'Handley found that the magneto–elastic constants may differ substantially from their respective bulk values near the surface region of a bulk sample [5].

Magneto–elastic coupling is the driving force for the well known effect of *magnetostriction* in bulk samples. Magnetostriction describes the strain induced by the magnetization of bulk samples. Ultrathin films, however, are rigidly bonded to a substrate, and are not free to change their length due to magnetization. Instead, magneto–elastic or magnetostrictive stresses evolve, and the resulting magnetostrictive strain depends on the rigidity of the substrate.

The magnetostrictive strain of Ni was found to shift to more negative values for decreasing film thickness [6, 7]. Permalloy, which is known to exhibit almost no magnetostriction in bulk samples showed a negative magnetostriction for films thinner than 7 nm, possibly inhibiting its use in spin-valve or magnetoresistive sensor applications [8]. Epitaxial film stress was found to change the sign and magnitude of the magneto–elastic coupling coefficients in nm epitaxial films [9, 10]. This short overview of the peculiar magneto–elastic coupling in ultrathin films shows that, in general, bulk magneto–elastic properties do not apply, and magneto–elastic data have to be measured for the film of interest. A versatile method that allows us to measure both film stress *and* magneto–elastic coupling from the curvature of a film–substrate composite is described. Film growth is intimately connected with the issue of lattice mismatch between film and substrate material. It is shown that an apparent thickness dependence of the magneto–elastic coupling coefficients can be ascribed to a strain-dependent correction of the respective bulk constants except for very thin films below 10 nm. It is proposed that for a film thickness below 10 nm additional so-called *surface corrections* of the magneto–elastic coupling have to be considered.

Although the magnetostrictive strains of the 3d-ferromagnetic elements Fe, Co, and Ni are rather small and reach only minute values of order 10^{-5} for Fe, the physical implications of the underlying principle of magneto–elastic coupling and magnetic anisotropy are profound. Tiny energy changes of only μeV per atom are a typical magnitude for anisotropy energies but nevertheless important magnetic properties like the direction of the easy axis of magnetization or the coercivity are governed by the magnetic anisotropy. Kittel introduced 50 years ago that the magnetostriction of bulk samples can be ascribed to a strain dependence of the magnetic anisotropy energy [11]. Thus, the study of magneto–elastic coupling is ultimately connected to an understanding of the relevant physical processes that determine magnetic anisotropy on an electronic level [12–14]. Only the advances in computational power and experimental techniques made it possible to study magnetostrictive effects even in monolayer thin films and some examples of the recent progress are presented.

The intimate relation between magnetism and lattice strain is well known from the discussion of magneto–volume instabilities [15] and especially from the so-called *Invar effect*. Invar originally described the almost negligible thermal expansion ($\alpha < 1 \times 10^{-6}$ K^{-1}) of ferromagnetic FeNi alloys upon heating below the Curie temperature [16]. Phenomenological models ascribe the almost nil thermal expansion of Invar to an increasing population of an energetically higher lying low-spin state, that has a smaller atomic volume and leads to a

cancellation of the positive thermal expansion with increasing temperature [17].

Magnetostriction is not necessarily small. Clark found a 'giant' room-temperature magnetostriction of order 10^{-3} in the rare-earth iron compound $TbFe_2$ [18] that led to the application of highly magnetostrictive alloys for sensor and actuator applications [19, 20].

This review concentrates on the issue of stress due to epitaxial misfit and its effect on the peculiar magneto–elastic coupling in ultrathin films. In the following section, the tensor character of strain and stress is taken into account to derive the stress–strain relations for various crystal orientations. Section 3 introduces the concept of *magneto–elastic coupling* and *magnetostrictive stress* which is more appropriate in the discussion of ultrathin films that are bonded to a substrate and therefore cannot show magnetostriction as known from bulk samples. Surface effects and strain dependence of the magneto–elastic coupling are discussed before a short compilation of recent *ab initio* calculations on magneto–elastic coupling concludes the chapter. Direct and indirect experimental techniques to investigate magneto–elastic coupling are briefly described in section 4, before stress measurements with samples that are clamped at only one end along their width to a manipulator, so-called *cantilevered* samples, are discussed in section 5. The impact of stress-driven structural changes on magnetism is corroborated by examples of epitaxial growth of Fe on W single crystal substrates, that are presented in section 6. Experimental evidence for strain-induced changes of the magneto–elastic coupling follows in section 7.

This review focuses on the relation between film strain and film stress which is necessary in order to compare experimental results of film stress with the expectations from lattice mismatch arguments and bulk magneto–elastic properties. Consequently, other important aspects of epitaxial growth and magnetism are not covered, and the reader is referred to the following reviews. At sub-monolayer coverages of epitaxial growth, surface-stress effects dominate the stress behaviour, and the role of surface stress for epitaxial growth has been reviewed by Ibach [21]. The strain analysis of epitaxial films from low-energy electron diffraction (LEED) experiments has been reviewed by Jona and Marcus in a series of publications [22–26]. The role of lattice mismatch for the formation of misfit dislocations has been reviewed by Matthews and Blakeslee [27–29] and by van der Merwe [30–33] and in the book by Markov [34]. Growth and properties of epitaxial films are covered in [35]. The magnetic properties of ultrathin films were reviewed by Falicov *et al* [36], Gradmann [37] and Allenspach [38] and in the two volumes of *Ultrathin Magnetic Structures* [39, 40]. Reviews on the related topics of magneto-optical effects [41], scanning tunnelling microscopy (STM) [42] and ferromagnetic resonance of ultrathin metallic layers [43] were recently published in this journal.

2. Strain and stress in epitaxial growth

Film growth is always connected with the issue of lattice mismatch η, given by the difference between the lattice constant of the film material a_F and the lattice constant of the substrate a_S as $\eta = (a_S - a_F)/a_F$. It determines the strain in an epitaxial film. In this review we limit the discussion to cases of epitaxy, where the unit cells of the substrate and the film differ only by a scaling factor, that might be constant within all directions of the film plane (e.g. bcc film on bcc substrate), or that might be different along two orthogonal directions within the film plane (e.g. the Nishiyama–Wassermann growth mode of an fcc film material on a bcc(110) substrate). The goal of this section is to derive equations for the perpendicular strain in the epitaxial film and for the biaxial stress that results from the in-plane epitaxial strain. The magnitude of the in-plane strain η and the perpendicular strain $\epsilon_\perp$ is important for the discussion of the magneto–elastic contribution to the magnetic anisotropy [14, 44–56]. A strain analysis for the cases of general epitaxy is given in the review by Jona and Marcus [22, 25].

First, we derive the equations for the elastic energy densities for cubic and hexagonal film materials. It is instructive to calculate the elastic energy density in epitaxially strained films as the magnitude of the strain energy is of key importance in the discussion of structural and morphological changes in ultrathin films. We shall see that the strain energy can be as high as several tenths of an eV which makes the elastic strain energy an important energy contribution in epitaxial growth.

The starting point for our discussion is the expression for the elastic energy density f_{el} as a function of the elements of the elastic stiffness tensor c_{ijkl} and the symmetric strain tensors ϵ_{ij}, ϵ_{kl} [57],

$$f_{\mathrm{el}} = \tfrac{1}{2} c_{ijkl} \epsilon_{ij} \epsilon_{kl}. \tag{2.1}$$

The subscripts i, j, k, l run from 1 to 3, and it is understood that the right-hand side of (2.1) is summed over all subscripts, which gives a total of 3^4 terms. Fortunately, the symmetry of the elasticity tensor $\boldsymbol{c}$ and the strain tensor $\boldsymbol{\epsilon}$ allow for a considerable simplification that leads to the so-called contracted *Voigt* notation. The first two subscripts and the last two subscripts are contracted according to the following scheme [58] to obtain the much more convenient matrix notation:

$$\begin{array}{lcccccc} \text{tensor notation:} & 11 & 22 & 33 & 23, 32 & 31, 13 & 12, 21 \\ \text{matrix notation:} & 1 & 2 & 3 & 4 & 5 & 6. \end{array} \tag{2.2}$$

Note that the subscripts run from 1 to 6 in the matrix notation and that factors of two are inserted in the definition of the off-diagonal elements [58], i.e. $\epsilon_4 = 2\epsilon_{23}$, $\epsilon_5 = 2\epsilon_{13}$, $\epsilon_6 = 2\epsilon_{12}$. The factor two is due to the application of a symmetric strain tensor ϵ [59]. We stick to the compact matrix notation to derive the stress–strain relations. However, when we calculate the directional dependence of the elastic properties in the next section, we have to return to the tensor notation to perform the necessary transformations. The most significant simplification of (2.1) follows from the symmetry of the crystal classes: only three independent elastic constants are needed to describe the elastic properties of the cubic class, whereas four elastic constants are required for the hexagonal class. The non-zero elements of the elastic stiffness matrix c_{ij} are given for the cubic class:

$$c_{ij}^{\mathrm{cubic}} = \begin{pmatrix} c_{11} & c_{12} & c_{12} & 0 & 0 & 0 \\ c_{12} & c_{11} & c_{12} & 0 & 0 & 0 \\ c_{12} & c_{12} & c_{11} & 0 & 0 & 0 \\ 0 & 0 & 0 & c_{44} & 0 & 0 \\ 0 & 0 & 0 & 0 & c_{44} & 0 \\ 0 & 0 & 0 & 0 & 0 & c_{44} \end{pmatrix} \tag{2.3}$$

and for the hexagonal class [58]:

$$c_{ij}^{\mathrm{hexagonal}} = \begin{pmatrix} c_{11} & c_{12} & c_{13} & 0 & 0 & 0 \\ c_{12} & c_{11} & c_{13} & 0 & 0 & 0 \\ c_{13} & c_{13} & c_{33} & 0 & 0 & 0 \\ 0 & 0 & 0 & c_{44} & 0 & 0 \\ 0 & 0 & 0 & 0 & c_{44} & 0 \\ 0 & 0 & 0 & 0 & 0 & \frac{1}{2}(c_{11} - c_{12}) \end{pmatrix}. \tag{2.4}$$

The same matrix positions are occupied in the contracted representation of the elastic compliance matrix s_{ij}. The matrix elements s_{ij} are given in terms of c_{ij} for both cubic and hexagonal systems in the appendix. Values of the elastic properties of various ferromagnetic elements and of some typical substrate materials are given in table 1.

Thus, we can finally quote the expressions for the elastic energy density of the cubic and the hexagonal class, as obtained from expanding (2.1) in the matrix notation $f_{\mathrm{elastic}} = \frac{1}{2} c_{ij} \epsilon_i \epsilon_j$,

Table 1. Elastic stiffness constants c_{ij} (GPa) and elastic compliance constants s_{ij} (TPa)$^{-1}$ from [60, 61]. Young's modulus Y (GPa) and Poisson's ratio ν for cubic and hexagonal elements. Y and ν are calculated from (2.15) for cubic elements for directions parallel to the crystal axes and for hcp Co for directions within the basal plane.

Element	c_{11}	c_{12}	c_{44}	c_{13}	c_{33}	s_{11}	s_{12}	s_{44}	s_{13}	s_{33}	Y	ν
hcp Co	307	165	75.5	103	358	4.73	−2.31	13.2	−0.69	3.19	211	0.49
fcc Co	242	160	128			8.81	−3.51	7.83			114	0.40
bcc Fe	229	134	115			7.64	−2.81	8.71			131	0.37
fcc Ni	249	152	118			7.53	−2.86	8.49			133	0.38
Si	165	63	79.1			7.73	−2.15	12.7			129	0.28
MgO	293	92	155			4.01	−0.96	6.48			249	0.24
bcc Mo	465	163	109			2.63	−0.68	9.20			380	0.26
bcc W	517	203	157			2.49	−0.7	6.35			402	0.28

$i, j = 1, 2, \ldots, 6$:

$$f_{\text{elastic}}^{\text{cubic}} = \tfrac{1}{2}c_{11}(\epsilon_1^2 + \epsilon_2^2 + \epsilon_3^2) + c_{12}(\epsilon_1\epsilon_2 + \epsilon_2\epsilon_3 + \epsilon_1\epsilon_3) + \tfrac{1}{2}c_{44}(\epsilon_4^2 + \epsilon_5^2 + \epsilon_6^2) \tag{2.5}$$

$$f_{\text{elastic}}^{\text{hexagonal}} = \tfrac{1}{2}c_{11}(\epsilon_1^2 + \epsilon_2^2) + \tfrac{1}{2}c_{33}\epsilon_3^2 + c_{12}\epsilon_1\epsilon_2 + c_{13}(\epsilon_1\epsilon_3 + \epsilon_2\epsilon_3) + \tfrac{1}{2}c_{44}(\epsilon_4^2 + \epsilon_5^2) + \tfrac{1}{4}(c_{11} - c_{12})\epsilon_6^2. \tag{2.6}$$

The elastic energy density of an epitaxial film can be calculated directly from (2.5) and (2.6) if the film coordinate system is oriented parallel to the orthogonal crystal coordinate system in which the elastic constants c_{ij} are defined. For cubic film materials, this is the case for the (100)-orientation of both fcc and bcc elements, for hexagonal film materials, this is the case for the (0001)-orientation, with the c-axis parallel to the z-direction. Expressions for the elastic energy density for cubic films with (111)- or (110)-orientations, and for hexagonal films with the $(11\bar{2}0)$-orientation are derived below.

As an example, we discuss the pseudomorphic growth of Fe on W(100). The in-plane strains ϵ_1 and ϵ_2 are given by the epitaxial misfit $\eta = 0.104$ that follows from the lattice constants $a_{\text{Fe}} = 2.866$ Å and $a_{\text{W}} = 3.165$ Å [62]. For this case of simple epitaxy, there are no shear strains, $\epsilon_4 = \epsilon_5 = \epsilon_6 = 0$, and the strain perpendicular to the film surface ϵ_3 is found by minimizing the elastic energy density (2.5) by varying ϵ_3:

$$\frac{\partial f_{\text{elastic}}^{\text{cubic}}}{\partial \epsilon_3} = c_{11}\epsilon_3 + c_{12}(\epsilon_1 + \epsilon_2) = \tau_3. \tag{2.7}$$

Note that the strain derivative of the elastic energy density with respect to ϵ_i gives the stress τ_i in the direction i. Setting the stress perpendicular to the film $\tau_3 = 0$ gives the vertical strain ϵ_3:

$$\epsilon_3 = -\frac{c_{12}}{c_{11}}(\epsilon_1 + \epsilon_2) = -\frac{\nu}{1-\nu}(\epsilon_1 + \epsilon_2). \tag{2.8}$$

The assumption of zero stress in the direction perpendicular to the film plane is reasonable as the film atoms are free to move along the film normal to minimize their elastic energy. This degree of freedom to minimize the elastic energy is not available for atomic displacements parallel to the film plane in the case of pseudomorphic growth. Here, the strong bonds to the substrate fix the lateral positions of the film atoms at sites that correspond to a continuation of the substrate. However, once the elastic energy becomes too large and the pseudomorphic growth is replaced by the introduction of misfit distortions, the in-plane pseudomorphic registry between film atoms and substrate atoms is no longer given and the in-plane strains are not known *a priori*.

In (2.8), we have introduced Poisson's ratio ν. The in-plane strains induce a perpendicular strain ϵ_3 that is not simply given by ν, but is rather a function of ν. For Fe(100)-films, $c_{11} = 229$ GPa, $c_{12} = 134$ GPa, $\nu = c_{12}/(c_{11} + c_{12}) = 0.37$ and for pseudomorphic Fe films on W(100), the perpendicular strain follows as: $\epsilon_3 = -0.119$. The in-plane tensile strain of $\eta = 10.4\%$ should result in a 11.9% contraction perpendicular to the film. The corresponding relative change of the atomic volume is given by the sum of the diagonal elements of the strain tensor [58], $\Delta V/V = (\epsilon_1 + \epsilon_2 + \epsilon_3) = 0.083$. The epitaxial misfit strain induces an increase of the atomic volume of the Fe atoms by more than 8%. The implications of a misfit-induced perpendicular strain and of the resulting change of the atomic volume are of great interest in the current discussion of epitaxial growth in view of the epitaxial path [26] and for the theoretical aspects of magnetism [15].

Now, the elastic energy density can be expressed as a function of the in-plane strains ϵ_1 and ϵ_2:

$$f_{\text{elastic}}^{\text{cubic}} = \tfrac{1}{2}c_{11}(\epsilon_1^2 + \epsilon_2^2) - \frac{c_{12}^2}{2c_{11}}(\epsilon_1 + \epsilon_2)^2 + c_{12}\epsilon_1\epsilon_2. \tag{2.9}$$

Inserting the values for c_{ij} from table 1 and taking $\epsilon_1 = \epsilon_2 = 0.104$ we calculate an elastic energy density for the pseudomorphic Fe film of 2.1 GJ m^{-3}. This amounts to a considerable strain energy per Fe atom of 200 meV/atom, which is more than a factor of 10 000 larger than the magnetic anisotropy of Fe of $K_1 = 4$ μeV/atom [63]. This is a very high energy contribution due to the strained growth and we will see that the elastic strain energy is so large that only three layers grow pseudomorphically before misfit distortions are introduced in the film to reduce the strain energy. The introduction of misfit distortions can be detected by stress measurements that are discussed in section 6. To derive the expression for the film stress, we have to calculate the partial derivative of the elastic energy with respect to the in-plane strain:

$$\tau_1 = \frac{\partial f_{\text{elastic}}^{\text{cubic}}}{\partial \epsilon_1} = \left(c_{11} - \frac{c_{12}^2}{c_{11}}\right)\epsilon_1 + \left(c_{12} - \frac{c_{12}^2}{c_{11}}\right)\epsilon_2. \tag{2.10}$$

The in-plane stress is isotropic and $\tau_1 = \tau_2 = 21$ GPa. This is a tremendous film stress that is more than a factor of ten higher than the yield strength of CrNi-steel. We will see in section 7 that a stress of 10 GPa is measured for the first three monolayers that grow pseudomorphically. Whether the discrepancy between the calculated stress and the measured stress by a factor of two is due to the questionable application of bulk elasticity data for Fe monolayers, or whether the non-layer-by-layer like growth mode of Fe on W(100), as found in scanning tunnelling microscopy (STM) experiments [64], causes the film stress to be lower than expected remains to be investigated.

The presented application of continuum elasticity to discuss monolayer properties is certainly a severe simplification and one has to worry what the minimum film thickness is where continuum elasticity applies [65]. An indirect hint toward the minimum thickness of the applicability of continuum elasticity might be taken from the results of electron spectroscopy experiments that suggest that at least the electronic structure of ultrathin films is very similar to that of bulk samples when the film thickness exceeds five layers [66–68]. Assuming that within the 3d metal film the bonds are predominantly formed by the 3d and 4s electrons [69,70], a bulklike electronic d-band structure should be a necessary requirement for the application of bulk atomic distances and elastic properties in ultrathin films. *Ab initio* calculations of the strain dependence of the total energy of several monolayer thin slabs are currently under way [71] and should elucidate the contributions of surface-stress and interface effects on the elastic properties of monolayers. Electronic surface and interface states have been clearly identified in electron spectroscopy [72, 73] and their possible impact on the elastic properties should not be neglected. In addition, the surface stress of the film–substrate composite has been

identified in experimental and theoretical investigations as an important factor that determines the stress in the (sub)monolayer range [21]. In conclusion, we suggest that it is physically sound to apply continuum elasticity models to ultrathin films that are at least 5–7 layers thick. Deviations from bulk behaviour have to be expected in the first monolayers. However, an *ab initio* description of the atomic origin of forces at surfaces and interfaces is still in its infancy and no comprehensive account of valid physical concepts can presently be presented [21].

2.1. Directional dependence of elastic properties

Unfortunately, many interesting film–substrate combinations do not result in cubic (100)-films that are discussed in section 2 and the directional dependence of the elastic properties has to be considered. This is most easily done by taking advantage of the tensor character of both elastic constants and strains. We present expressions for the elastic energy density, the strain ϵ_3 as a function of the in-plane strains, ϵ_1 and ϵ_2, the in-plane stresses, τ_1 and τ_2, as a function of the in-plane strains and of both Young's modulus Y and Poisson's ratio ν for cubic (100)-, (110)- and (111)-films, and for hexagonal (0001)- and $(11\bar{2}0)$-films. We will see, for example, that Y might change by almost 50% for different directions within the (110)-plane. Thus, a derivation of the appropriate directional dependence is clearly called for to allow for a comparison between experimental results and the prediction of continuum elasticity.

There are two ways to take the directional dependence of the elastic properties into account. (i) Transformation of the strain tensor: a primed film coordinate system is set up in which the film strains ϵ_1' and ϵ_2' describe the epitaxial misfit strain in the film plane, and ϵ_3' describes the strain perpendicular to the film plane. A transformation matrix with elements a_{ij} is derived by expressing the primed film directions as a function of the crystal directions. Finally, the crystal strains are expressed as a function of the film strains, and (2.5) and (2.6) can be used with the strains ϵ_i replaced with the appropriate expressions in terms of the ϵ_j'. The partial derivative of the elastic energy density with respect to the film strains gives the film stresses in the film coordinate system. The benefit of this approach is that only the strain tensor has to be transformed, which can be easily done by the respective matrix multiplication $\boldsymbol{\epsilon} = \boldsymbol{a}^{\mathrm{T}}\boldsymbol{\epsilon}'\boldsymbol{a}$ that uses the transpose $\boldsymbol{a}^{\mathrm{T}}$ of the transformation matrix $\boldsymbol{a}$. The disadvantage is that one does not obtain the directional dependence of the elastic constants directly. (ii) Transformation of the elastic stiffness or of the elastic compliance tensor: for this approach, one transforms the elastic stiffness constants c_{ijkl} or the elastic compliance constants s_{ijkl} by the appropriate tensor transformation with the transformation matrix $\boldsymbol{a}$. The primed elastic constants of the film system can then be expressed as a function of the elastic constants of the crystal system:

$$c'_{ijkl} = a_{im}a_{jn}a_{ko}a_{lp}c_{mnop}, \qquad i, j, \ldots, p = 1, 2, 3. \tag{2.11}$$

Each primed elastic constant is given by 3^4 terms. The strains do not need to be transformed and can be taken directly from the film system. The benefit of this approach is that one can derive the directional dependence of single elastic constants and of composite elastic properties like Young's modulus Y and Poisson's ratio ν directly. Once these transformations have been performed we can return to the contracted matrix notation which allows a very concise description of the elastic properties:

$$\tau_i' = c_{ij}'\epsilon_j', \tag{2.12}$$

$$\epsilon_i' = s_{ij}'\tau_j', \qquad i, j = 1, 2, \ldots, 6. \tag{2.13}$$

Note that for the cases of simple epitaxy that we study here, no shear strains are found in the film system, $\epsilon_4' = \epsilon_5' = \epsilon_6' = 0$, and ϵ_3' is obtained by setting $\tau_3' = 0$. Expanding (2.13) for

ϵ_1' and rearranging the terms gives

$$\tau_1' = \frac{1}{s_{11}'}\epsilon_1' - \frac{s_{12}'}{s_{11}'}\tau_2'. \tag{2.14}$$

Comparing (2.14) with the definition of Young's modulus Y and Poisson's ratio ν [59] $\tau_1 = Y\epsilon_1 + \nu\tau_2$ shows that Y' and ν' can be expressed by the elastic compliances in the film system:

$$Y' = \frac{1}{s_{11}'} \qquad \nu' = -\frac{s_{12}'}{s_{11}'}. \tag{2.15}$$

To perform the tensor transformation of the elastic compliance of the cubic system, the directions in which Y and ν are needed are specified by the direction cosines $a_{11} = l_1$, $a_{12} = l_2$, $a_{13} = l_3$ and $a_{21} = m_1$, $a_{22} = m_2$, $a_{23} = m_3$. These direction cosines are given with respect to the crystal axes x, y and z. With reference to (2.14), the vector $\boldsymbol{l}$ is parallel to the strain ϵ_1', whereas the direction of $\boldsymbol{m}$ is perpendicular to ϵ_1' and gives the direction of τ_2' as the Poisson-type contribution to τ_1' [21, 58, 74]:

cubic:
$$1/Y' = s_{11}' = s_{1111}' = a_{1,m}a_{1,n}a_{1,o}a_{1,p}s_{mnop}^{\text{cubic}}$$
$$= s_{11} - 2(s_{11} - s_{12} - \tfrac{1}{2}s_{44})(l_1^2l_2^2 + l_1^2l_3^2 + l_2^2l_3^2) \tag{2.16}$$

cubic:
$$\nu' = -\frac{s_{12}'}{s_{11}'} = -\frac{s_{12} + (s_{11} - s_{12} - \frac{1}{2}s_{44})(l_1^2m_1^2 + l_2^2m_2^2 + l_3^2m_3^2)}{s_{11} - 2(s_{11} - s_{12} - \frac{1}{2}s_{44})(l_1^2l_2^2 + l_1^2l_3^2 + l_2^2l_3^2)}. \tag{2.17}$$

The important result of (2.16) is that the amount of elastic anisotropy for cubic elements depends on the directional factor $(l_1^2l_2^2 + l_1^2l_3^2 + l_2^2l_3^2)$ and on the magnitude of the anisotropy term $(s_{11} - s_{12} - \frac{1}{2}s_{44})$. The larger the anisotropy term, the larger the correction to s_{11}, and a pronounced elastic anisotropy results. To illustrate the different degrees of anisotropy for various elements, we plot in figure 1 a three-dimensional representation of the directional dependence of Y.

Only for W is the anisotropy term ≈ 0, and an almost isotropic Y results. For the other elements, pronounced anisotropies result, and Y is large along the $\langle 111\rangle$-directions for elements with a positive anisotropy term (Fe), or Y is large along the $\langle 100\rangle$-directions for elements with a negative anisotropy term (Mo), respectively. Figure 1 clearly shows that Y is *not* isotropic within the (100)-plane of cubic materials, but the following derivation of the elastic properties along selected directions reveals that $Y/(1-\nu)$, which determines the biaxial rigidity, *is* isotropic in (100)-planes. A cross section of Y along a (111)-plane reveals an isotropic Y, however, the value of Y is not simply given by $1/s_{11}$, as calculated in the next section.

For hexagonal elements, the different symmetry of the compliance tensor results in a different expression for the transformation:

hexagonal:
$$1/Y' = s_{11}' = s_{1111}' = a_{1,m}a_{1,n}a_{1,o}a_{1,p}s_{mnop}^{\text{hexagonal}}$$
$$= s_{11}(1 - l_3^2) + s_{33}l_3^4 + (s_{44} + 2s_{13})l_3^2(1 - l_3^2). \tag{2.18}$$

To account for the elastic anisotropy of the hexagonal elements, only the direction cosine l_3 between the c-axis and the direction under consideration matters. Y is isotropic in the basal plane, therefore figure 1(d) shows rotational symmetry around the c-axis.

2.2. Elastic properties of various epitaxial orientations

Young's modulus, Poisson's ratio, the stress–strain relations, the elastic energy density in terms of the in-plane strains ϵ_1 and ϵ_2 and the strain ratio $\epsilon_3/(\epsilon_1 + \epsilon_2)$ are given for some frequently used film orientations.

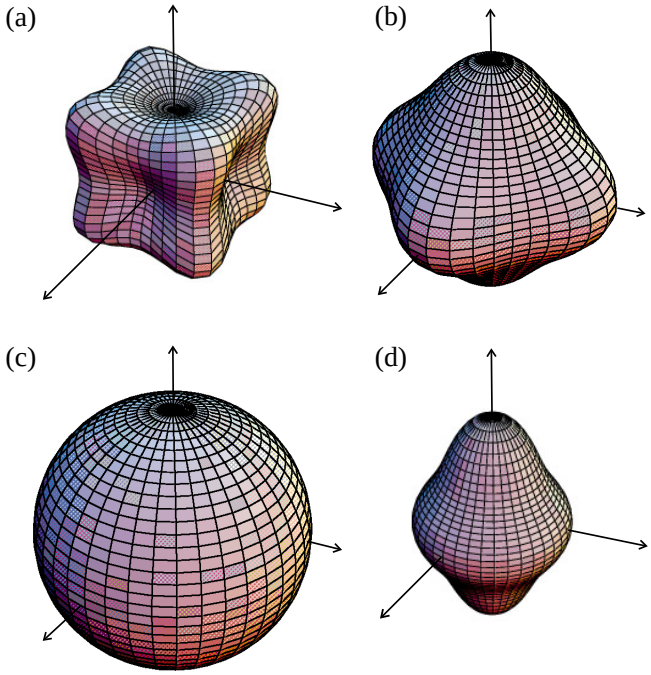

Figure 1. Anisotropy of Young's modulus Y, calculated from (2.16) and (2.18). The distance from the surface of the bodies to the centre of the bodies represents Y along that direction. (*a*) bcc Fe. (*b*) bcc Mo. (*c*) bcc W. (*d*) hcp Co. Note the pronounced anistropy for Fe and Mo versus the almost isotropic Y of W. For hcp Co, Y is isotropic in the basal plane, and a rotational symmetry around the *c*-axis results.

2.2.1. Cubic (100)-films. The in-plane strains are oriented along the directions of the crystal axes of the film material and no tensor transformations are necessary to obtain the stress–strain relations in the technical and in the compliance notation:

$$\tau_1 = Y\epsilon_1 + \nu\tau_2 \qquad \epsilon_1 = s_{11}\tau_1 + s_{12}\tau_2 \qquad \tau_1 = c_{11}\epsilon_1 + c_{12}\epsilon_2 + c_{12}\epsilon_3 \tag{2.19}$$

$$\tau_2 = Y\epsilon_2 + \nu\tau_1 \qquad \epsilon_2 = s_{11}\tau_2 + s_{12}\tau_1 \qquad \tau_2 = c_{12}\epsilon_1 + c_{11}\epsilon_2 + c_{12}\epsilon_3. \tag{2.20}$$

Solving these equations for the stresses τ_i gives:

$$\tau_1 = \frac{Y}{1-\nu^2}(\epsilon_1 + \nu\epsilon_2) \qquad \tau_1 = \frac{1}{(1-(\frac{s_{12}}{s_{11}})^2)}\frac{1}{s_{11}}\left(\epsilon_1 - \frac{s_{12}}{s_{11}}\epsilon_2\right) \tag{2.21}$$

$$\tau_2 = \frac{Y}{1-\nu^2}(\epsilon_2 + \nu\epsilon_1) \qquad \tau_2 = \frac{1}{(1-(\frac{s_{12}}{s_{11}})^2)}\frac{1}{s_{11}}\left(\epsilon_2 - \frac{s_{12}}{s_{11}}\epsilon_1\right). \tag{2.22}$$

Comparing the coefficients of ϵ_1 and ϵ_2 reveals that $Y = 1/s_{11} = (c_{11} + 2c_{12})(c_{11} - c_{12})/(c_{11} + c_{12})$ and $\nu = -s_{12}/s_{11} = c_{12}/(c_{11} + c_{12})$. The compliances s_{ij} can be expressed in terms of the elastic stiffness constants c_{ij}, as derived in the appendix. In the case of isotropic in-plane strain induced by the lattice mismatch η, $\epsilon_1 = \epsilon_2 = \eta$, and the simple relation $\tau = Y/(1-\nu)\eta$ results.

The strain ratio between the strain ϵ_3 normal to the film plane and the in-plane strains follows from the condition $\tau_3 = 0$, as discussed in section 2:

$$\frac{\epsilon_3}{\epsilon_1 + \epsilon_2} = -\frac{\nu}{1-\nu} = \frac{s_{12}}{s_{11} + s_{12}} = -\frac{c_{12}}{c_{11}}. \tag{2.23}$$

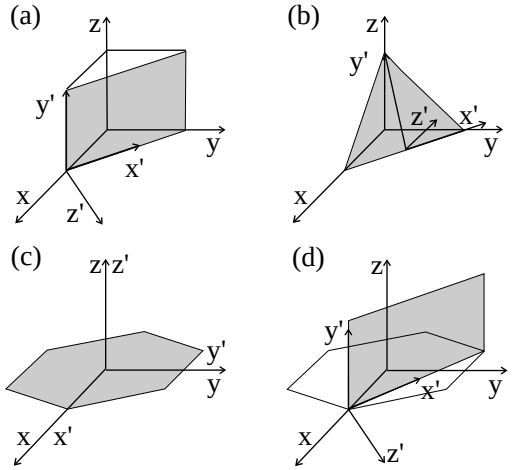

Figure 2. The grey-shaded areas show various film orientations. The un-primed crystal coordinate system and the primed film coordinate system are indicated. (*a*) Cubic-(110), (*b*) cubic-(111), (*c*) hexagonal-(0001), (*d*) hexagonal-(11$\bar{2}$0).

The elastic energy density for cubic elements with an (100)-orientation that are only strained in-plane, with all shear strains $\epsilon_4 = \epsilon_5 = \epsilon_6 = 0$, has been derived in (2.9):

$$f_{\text{elastic}}^{\text{cubic(100)}} = \tfrac{1}{2}c_{11}(\epsilon_1^2 + \epsilon_2^2) - \frac{c_{12}^2}{2c_{11}}(\epsilon_1 + \epsilon_2)^2 + c_{12}\epsilon_1\epsilon_2. \tag{2.24}$$

As we need the expressions for the elastic energy densities of the various film orientations for the discussion of the magneto–elastic coupling, we derive in the following the stress–strain relations from the transformations of the elastic energy density.

2.2.2. Cubic (110)-films. The (110)-orientation requires that the appropriate tensor transformation is performed, as one of the orthogonal in-plane directions does not coincide with a crystal axis. First, the transformation matrix $\boldsymbol{a}$ is derived from an analysis of the surface geometry in figure 2(*a*).

To obtain the elements of the transformation matrix $\boldsymbol{a}$, the primed film directions, x', y', z', have to be expressed as a function of the crystal directions x, y, z as unit vectors. The relations are arranged in form of a matrix, and the elements of $\boldsymbol{a}$ follow directly:

	x	y	z
x'	$\frac{-1}{\sqrt{2}}$	$\frac{1}{\sqrt{2}}$	0
y'	0	0	1
z'	$\frac{1}{\sqrt{2}}$	$\frac{1}{\sqrt{2}}$	0

$$a_{ij} = \begin{pmatrix} \frac{-1}{\sqrt{2}} & \frac{1}{\sqrt{2}} & 0 \\ 0 & 0 & 1 \\ \frac{1}{\sqrt{2}} & \frac{1}{\sqrt{2}} & 0 \end{pmatrix}. \tag{2.25}$$

Now, the tensor transformation for the strain can be performed,

$$\epsilon = a^{\mathrm{T}}\epsilon' a$$
$$\epsilon_{ij} = \begin{pmatrix} \frac{1}{2}(\epsilon_1' + \epsilon_3') & \frac{1}{2}(-\epsilon_1' + \epsilon_3') & 0 \\ \frac{1}{2}(-\epsilon_1' + \epsilon_3') & \frac{1}{2}(\epsilon_1' + \epsilon_3') & 0 \\ 0 & 0 & \epsilon_2' \end{pmatrix}, \tag{2.26}$$

and the values of ϵ are expressed in terms of the ϵ' in the expression of the elastic energy density of (2.5):

$$f_{\text{elastic}}^{(110)} = \tfrac{1}{4}c_{11}(\epsilon_1'^2 + 2\epsilon_2'^2 + 2\epsilon_1'\epsilon_3' + \epsilon_3'^2) + \tfrac{1}{4}c_{12}(\epsilon_1'^2 + 4\epsilon_1'\epsilon_2' + 2\epsilon_1'\epsilon_3' + 4\epsilon_2'\epsilon_3' + \epsilon_3'^2)$$

$$+\tfrac{1}{2}c_{44}(\epsilon_3' - \epsilon_1')^2. \tag{2.27}$$

Searching for the minimum of the elastic energy density with respect to ϵ_3' by setting $\partial f_{\text{elastic}}/\partial\epsilon_3' = 0$ gives the perpendicular strain

$$\epsilon_3' = -\frac{(c_{11} + c_{12} - 2c_{44})\epsilon_1' + 2c_{12}\epsilon_2'}{c_{11} + c_{12} + 2c_{44}}. \tag{2.28}$$

Finally, ϵ_3' is expressed in terms of the in-plane film strains ϵ_1' and ϵ_2', and the in-plane film stresses τ_1' and τ_2' are calculated from the partial derivatives of the elastic energy density.

$$f_{\text{elastic}}^{(110)} = \frac{4(c_{11} + c_{12})c_{44}\epsilon_1'^2 + 8c_{12}c_{44}\epsilon_1'\epsilon_2' + (c_{11}^2 - 2c_{12}^2 + c_{11}(c_{12} + 2c_{44}))\epsilon_2'^2}{2(c_{11} + c_{12} + 2c_{44})} \tag{2.29}$$

$$\tau_1' = \frac{\partial f_{\text{elastic}}^{(110)}}{\partial\epsilon_1'} = \frac{4(c_{11} + c_{12})c_{44}\epsilon_1' + 4c_{12}c_{44}\epsilon_2'}{c_{11} + c_{12} + 2c_{44}} \tag{2.30}$$

$$\tau_2' = \frac{\partial f_{\text{elastic}}^{(110)}}{\partial\epsilon_2'} = \frac{4c_{12}c_{44}\epsilon_1' + (c_{11}^2 - 2c_{12}^2 + c_{11}(c_{12} + 2c_{44}))\epsilon_2'}{c_{11} + c_{12} + 2c_{44}}. \tag{2.31}$$

Note the different prefactors for the in-plane strains that result in an anisotropic film stress even for isotropic strain $\epsilon_1' = \epsilon_2'$.

As an example we discuss the elastic properties of pseudomorphically strained Fe monolayers on W(110). Here the lattice mismatch η is isotropic, $\eta = \epsilon_1' = \epsilon_2' = 0.104$, and the Fe film is under tensile strain to accommodate the larger atomic distances on the W surface. Taking the elastic constants of bulk Fe, as given in table 1, a perpendicular compressive strain of $\epsilon_3' = -0.068$ results. The in-plane stress along $[\bar{1}10]$, $\tau_1' = 38.9$ GPa, is 41% larger than the in-plane stress along [001], $\tau_2' = 27.5$ GPa. The elastic energy density of the pseudomorphically strained Fe(110) film is 3.36 GJ m^{-3}, which gives a tremendous strain energy per Fe atom of 0.32 eV/atom. As discussed in section 6, the measured stress in the pseudomorphic region is 65 GPa along [001] and 44 GPa along $[\bar{1}10]$, respectively. These results indicate a considerable discrepancy between measured film stress and calculated stress, even for a coverage above 0.5 monolayers. However, the calculated stress anisotropy is also found in the experiments. We refer to the pronounced stress anisotropy later when we discuss the growth of elongated Fe islands for 1.5 ML Fe on W(110), see figure 13. The large strain energy of more than 0.3 eV/atom leads to the formation of misfit distortions already in the second layer of Fe, as discussed in section 6. The role of the film strains for the magnetic anisotropy is also discussed there.

2.2.3. Cubic (111)-films. Figure 2(*b*) indicates a film coordinate system, that leads to the following transformation matrix,

	x	y	z
x'	$\frac{-1}{\sqrt{2}}$	$\frac{1}{\sqrt{2}}$	0
y'	$\frac{-1}{\sqrt{6}}$	$\frac{-1}{\sqrt{6}}$	$\sqrt{\frac{2}{3}}$
z'	$\frac{1}{\sqrt{3}}$	$\frac{1}{\sqrt{3}}$	$\frac{1}{\sqrt{3}}$

$$a_{ij} = \begin{pmatrix} \frac{-1}{\sqrt{2}} & \frac{1}{\sqrt{2}} & 0 \\ \frac{-1}{\sqrt{6}} & \frac{-1}{\sqrt{6}} & \sqrt{\frac{2}{3}} \\ \frac{1}{\sqrt{3}} & \frac{1}{\sqrt{3}} & \frac{1}{\sqrt{3}} \end{pmatrix}, \tag{2.32}$$

from which the relations between the crystal strains and the film strains follows as

$$\epsilon_{ij} = \begin{pmatrix} \frac{1}{2}\epsilon_1' + \frac{1}{6}\epsilon_2' + \frac{1}{3}\epsilon_3' & -\frac{1}{2}\epsilon_1' + \frac{1}{6}\epsilon_2' + \frac{1}{3}\epsilon_3' & \frac{1}{3}(-\epsilon_2' + \epsilon_3') \\ -\frac{1}{2}\epsilon_1' + \frac{1}{6}\epsilon_2' + \frac{1}{3}\epsilon_3' & \frac{1}{2}\epsilon_1' + \frac{1}{6}\epsilon_2' + \frac{1}{3}\epsilon_3' & \frac{1}{3}(-\epsilon_2' + \epsilon_3') \\ \frac{1}{3}(-\epsilon_2' + \epsilon_3') & \frac{1}{3}(-\epsilon_2' + \epsilon_3') & \frac{2}{3}\epsilon_2' + \frac{1}{3}\epsilon_3' \end{pmatrix}. \tag{2.33}$$

The elastic energy density is

$$f_{\text{elastic}}^{(111)} = c_{11}((\tfrac{1}{2}\epsilon_1' + \tfrac{1}{6}\epsilon_2' + \tfrac{1}{3}\epsilon_3')^2 + (\tfrac{2}{3}\epsilon_2' + \tfrac{1}{3}\epsilon_3)^2) + c_{12}((\tfrac{1}{2}\epsilon_1' + \tfrac{1}{6}\epsilon_2' + \tfrac{1}{3}\epsilon_3')^2 + 2(\tfrac{1}{2}\epsilon_1' + \tfrac{1}{6}\epsilon_2' + \tfrac{1}{3}\epsilon_3')(\tfrac{2}{3}\epsilon_2' + \tfrac{1}{3}\epsilon_3)) + 2c_{44}((-\tfrac{1}{2}\epsilon_1' + \tfrac{1}{6}\epsilon_2' + \tfrac{1}{3}\epsilon_3')^2 + 4(-\tfrac{1}{3}\epsilon_2' + \tfrac{1}{3}\epsilon_3')), \tag{2.34}$$

and the strain ϵ_3' perpendicular to the film that is induced by the in-plane strains is given by:

$$\epsilon_3' = -\frac{(c_{11} + 2c_{12} - 2c_{44})}{c_{11} + 2c_{12} + 4c_{44}}(\epsilon_1' + \epsilon_2'). \tag{2.35}$$

The elastic energy density is given terms of the in-plane strains

$$f_{\text{elastic}}^{(111)} = \frac{1}{4}(c_{11} + c_{12} + 2c_{44})(\epsilon_1'^2 + \epsilon_2'^2) - \frac{(c_{11} + 2c_{12} - 2c_{44})^2}{6(c_{11} + 2c_{12} + 4c_{44})}(\epsilon_1' + \epsilon_2')^2 + \tfrac{1}{6}(c_{11} + 5c_{12} - 2c_{44})\epsilon_1'\epsilon_2', \tag{2.36}$$

and the in-plane stresses follow as

$$\tau_i' = \left(\frac{1}{2}c_{11} + \frac{1}{2}c_{12} + c_{44} - \frac{1}{3}\frac{(c_{11} + 2c_{12} - 2c_{44})^2}{c_{11} + 2c_{12} + 4c_{44}}\right)\epsilon_i' + \left(\frac{1}{6}c_{11} + \frac{5}{6}c_{12} - \frac{1}{3}c_{44} - \tfrac{1}{3}\frac{(c_{11} + 2c_{12} - 2c_{44})^2}{c_{11} + 2c_{12} + 4c_{44}}\right)\epsilon_j' \tag{2.37}$$

with $i = 1$, $j = 2$ and $i = 2$, $j = 1$.

2.2.4. Hexagonal (0001)-films. The expression for the elastic energy density was derived in (2.6) and no transformations are necessary for this orientation where the direction of the film coordinate system is indicated by figure 2(*c*):

$$f_{\text{elastic}}^{(0001)} = \tfrac{1}{2}c_{11}(\epsilon_1^2 + \epsilon_2^2) + \tfrac{1}{2}c_{33}\epsilon_3^2 + c_{12}\epsilon_1\epsilon_2 + c_{13}(\epsilon_1\epsilon_3 + \epsilon_2\epsilon_3). \tag{2.38}$$

Here, $\epsilon_4 = \epsilon_5 = \epsilon_6 = 0$ was set due to the limitation to cases of simple epitaxy. The perpendicular strain follows as

$$\epsilon_3 = -\frac{c_{13}}{c_{33}}(\epsilon_1 + \epsilon_2), \tag{2.39}$$

the elastic energy density as function of the in-plane strains is

$$f_{\text{elastic}}^{(0001)} = \frac{1}{2}c_{11}(\epsilon_1^2 + \epsilon_2^2) + c_{12}\epsilon_1\epsilon_2 - \frac{c_{13}^2}{2c_{33}}(\epsilon_1 + \epsilon_2)^2 \tag{2.40}$$

and the in-plane stress is given by

$$\tau_i = \left(c_{11} - \frac{c_{13}^2}{c_{33}}\right)\epsilon_i + \left(c_{12} - \frac{c_{13}^2}{c_{33}}\right)\epsilon_j, \tag{2.41}$$

with $i = 1$, $j = 2$ and $i = 2$, $j = 1$.

2.2.5. Hexagonal $(11\bar{2}0)$-films. Figure 2(*d*) shows that one film direction is parallel to the *c*-axis, with the other film direction running in the basal plane. The transformation matrix can be written as

$$a = \begin{pmatrix} -\frac{\sqrt{3}}{2} & \frac{1}{2} & 0 \\ 0 & 0 & 1 \\ \frac{1}{2} & \frac{\sqrt{3}}{2} & 0 \end{pmatrix} \tag{2.42}$$

and the elastic energy density follows

$$f_{\text{elastic}}^{(11\bar{2}0)} = \tfrac{1}{2}c_{11}(\epsilon_1'^2 + \epsilon_3'^2) + c_{12}\epsilon_1'\epsilon_3' + c_{13}(\epsilon_1' + \epsilon_3')\epsilon_2' + \tfrac{1}{2}c_{33}\epsilon_2'^2. \tag{2.43}$$

The strain perpendicular to the film plane is

$$\epsilon_3' = -\frac{c_{12}\epsilon_1' + c_{13}\epsilon_2'}{c_{11}} \tag{2.44}$$

and the elastic energy density can be expressed as function of the in-plane strains

$$f_{\text{elastic}}^{(11\bar{2}0)} = \frac{1}{2}\left(c_{11} - \frac{c_{12}^2}{c_{11}}\right)\epsilon_1'^2 + \frac{1}{2}\left(c_{33} - \frac{c_{13}^2}{c_{11}}\right)\epsilon_2'^2 + \left(c_{13} - \frac{c_{12}c_{13}}{c_{11}}\right)\epsilon_1'\epsilon_2' \tag{2.45}$$

and the in-plane stresses follow as

$$\tau_1' = \left(c_{11} - \frac{c_{12}^2}{c_{11}}\right)\epsilon_1' + \left(c_{13} - \frac{c_{12}c_{13}}{c_{11}}\right)\epsilon_2' \tag{2.46}$$

$$\tau_2' = \left(c_{13} - \frac{c_{12}c_{13}}{c_{11}}\right)\epsilon_1' + \left(c_{33} - \frac{c_{13}^2}{c_{11}}\right)\epsilon_2'. \tag{2.47}$$

As an example, we discuss the growth of Co on W(100). The Co surface cell indicated in figure 2(*d*) is rotated by $\pi/4$ with respect to the W [001]-direction to fit the W surface cell with in-plane strains of $\epsilon_1' = 0.03$ and $\epsilon_2' = 0.09$. This epitaxial orientation results in a strain perpendicular to the film plane of $\epsilon_3' = -0.047$ and induces in-plane film stresses of $\tau_1' = 11$ GPa and $\tau_2' = 31$ GPa.

3. Magneto–elastic coupling

In the last section it was shown that the elastic energy density depends on the orientation of the strains with respect to the cubic axes. In ferromagnetic materials further terms contribute to the energy density. These terms depend on the orientation of the magnetization M, as specified by the direction cosines α_i between the direction of magnetization and the cubic axes. For example, the work done by magnetizing a crystal in an external magnetic field H is given by $\int H\mathrm{d}M$ and depends on the direction in which the sample is magnetized. This effect is due to the so-called magneto–crystalline anisotropy which has its origin in the spin–orbit coupling of the valence electrons of the sample. However, in addition to this directional dependence of the magnetic anisotropy, the magnetic properties depend on the overlap of wavefunctions which leads to a strain dependence of the magnetic anisotropy. A well known example for the strain dependence of magnetism is the effect of magnetostriction, which describes the change of the dimensions of a sample due to the magnetization process. Obviously, a sample can lower its energy by changing its length l in the magnetization process until elastic forces balance the magnetostrictive stress. The resulting magnetostrictive strains $\lambda = \Delta l/l$ are of order 10^{-5} for Fe [63] but can reach values as high as 10^{-3} for FeTb alloys [75].

Following Kittel [11] and Lee [2], the starting point in the discussion of strain-dependent magnetic properties is the magneto–elastic energy density f_{me}, with

$$f_{\text{me}}^{\text{cubic}} = B_1(\epsilon_1\alpha_1^2 + \epsilon_2\alpha_2^2 + \epsilon_3\alpha_3^2) + B_2(\epsilon_4\alpha_2\alpha_3 + \epsilon_5\alpha_1\alpha_3 + \epsilon_6\alpha_1\alpha_2) + \cdots \tag{3.1}$$

for a cubic system. The direction cosines of the magnetization with respect to the cubic axes are given by α_i, the strains ϵ_i are measured along the cubic axes. Equation (3.1) describes how the magnetization direction interacts with the strains to result in a magneto–elastic energy density that is given by the so-called magneto–elastic coupling coefficients B_1 and B_2. The dots indicate that higher-order terms in α_i, that are discussed, for example, by Becker and

Döring [76] or Carr [77], have been neglected. Higher-order terms in ϵ_i will be introduced later, when we discuss the deviation of the magneto–elastic coupling in ultrathin epitaxial films from the respective bulk values.

According to Kittel [11], the magneto–elastic coupling coefficients can be regarded as strain derivatives of the magnetic anisotropy energy density and calculations of the magnetic anisotropy can be exploited to determine the magneto–elastic coupling coefficients from first principles. *Ab initio* calculations of the anisotropy energy as a function of strain determine the magneto–elastic coupling coefficients directly. This approach has been employed to calculate the magneto–elastic coupling in Co monolayers [78], and to derive the magnetostriction of bulk Ni from fully relativistic calculations [13], and to exploit the magneto–elastic coupling in Ni monolayers [14]. A discussion of magneto–elastic coupling based on symmetry considerations is given in the articles by Mason [79, 80], Döring and Simon [81] and in the book by Trémolet de Lacheisserie [82].

The expression for the magneto–elastic energy density $f_{\rm me}$ in (3.1) is a function of the strain ϵ_i. The most important consequence of the strain dependence of $f_{\rm me}$ is that magneto–elastic *stresses* are inherently connected with the concept of magneto–elastic coupling. The observation of magnetostriction in bulk samples is a consequence of the magneto–elastic stress that acts to strain the sample until it is balanced by the restoring elastic forces. The driving force for this magnetostrictive strain is the minimization of the total energy of the sample in the magnetization process. A lowering of the sum of elastic and magneto–elastic energy by a non-zero strain is always possible as the magneto–elastic energy contribution depends linearly on the strains in the approximation given above. For bulk Fe, B_1 is negative ($B_1 = -0.253$ meV/atom) and Fe expands upon magnetization along a cubic axis ($\lambda_{100} = 24 \times 10^{-6}$). A positive B_1 is found for Ni, and consequently Ni contracts upon magnetization along a cubic axis. Most experimental data on the magneto–elastic coupling coefficients are obtained from measurements of the magnetostrictive strains λ of bulk samples, and the B_i are calculated from (3.2).

Before we discuss the magneto–elastic coupling in epitaxial films we recall how the expressions for the magnetostrictive strain in bulk samples are derived. To determine the so-called magnetostriction of bulk samples one has to find the strains ϵ_i that minimize the sum of the the magneto–elastic energy density, $f_{\rm me}$ (3.1), and of the elastic energy density, $f_{\rm elastic}$(2.5) [2, 11, 83]. This minimization procedure is equivalent to the condition, that the magnetostrictive stresses, as obtained by the partial derivatives of $f_{\rm me}$ with respect to the strains, are cancelled by the elastic stresses that evolve due to the strain in the sample. The relations between the magnetostrictive strains and the magneto–elastic coupling coefficients are used to define the relations between the so-called magnetostriction constants λ_{100}, λ_{111} and B_1, B_2 [2, 11, 83]:

$$\lambda_{100} = -\frac{2}{3}\frac{B_1}{(c_{11} - c_{12})}, \qquad \lambda_{111} = -\frac{1}{3}\frac{B_2}{c_{44}}. \tag{3.2}$$

The prefactors $\frac{2}{3}$ and $\frac{1}{3}$ enter, because one defines the magnetostriction constants λ_{100} (λ_{111}) as the relative change in length that one measures along [100] ([111]) due to the magnetization along [100] ([111]) *starting from an ideal demagnetized state*. This *demagnetized* state is assumed to be characterized by an isotropic distribution of the magnetization directions along the easy axes. For both Fe and Ni, this introduces factors of $\alpha_i^2(\text{demag}) = \frac{1}{3}$ and $\alpha_i\alpha_j(\text{demag}) = 0$ in (3.1) of the demagnetized reference state. The magneto–elastic coupling coefficients B_1 and B_2 can then be calculated from the magnetostrictive strains and from the elastic constants c_{ij} of bulk samples. To avoid the experimental uncertainty of an ideal demagnetized state as the reference, magnetostriction experiments of bulk samples are usually

Table 2. Room temperature values of λ_{100} and λ_{111} from [63], with the relations given in [2]. Data for fcc Co are extrapolated from measurements on PdCo alloys [91,92]. The B_i are calculated with (3.2). $\lambda_A, \ldots, \lambda_D$ are room-temperature values from [89], the B_i are calculated from (3.4). All B_i in MJ m^{-3}, all λ in 10^{-6}.

Element	B_1	B_2	λ_{100}	λ_{111}	B_3	B_4	λ_A	λ_B	λ_c	λ_D
bcc Fe	−3.43	7.83	24.1	−22.7						
fcc Co	−9.2	7.7	75	−20						
fcc Ni	9.38	10	−64.5	−28.3						
hcp Co	−8.1	−29			28.2	29.4	−50	−107	126	−105

performed by measuring the change of the magnetostrictive strain while the magnetization is rotated between two well-defined directions. Several authors derive procedures of how to orient the strain measurement direction in certain crystal planes and the direction of magnetization to obtain the magnetostriction constants [84–86]. This simplest description of anisotropic magnetostriction in cubic materials requires only two constants, and the use of higher-order terms in the direction cosines of magnetization α_i in (3.1) is *not* necessary due to the small magnitude of these terms that do not exceed the experimental uncertainty of the magnetostriction measurement [63, 84–87].

The description of the anisotropic magnetostriction in hexagonal crystals up to the second order in the direction cosine of magnetization requires four magneto–elastic coupling coefficients, or four magnetostriction constants, $\lambda_A, \ldots, \lambda_D$. Mason has derived the expressions for the magnetostrictive strain in an hexagonal crystal as a function of the direction of magnetization using four magnetostriction constants based on a phenomenological description that took the symmetry of the hexagonal system into account [80]. Experimental procedures to determine the four magnetostriction constants are given by Bozorth [88] and Hubert *et al* [89]. For example, λ_C describes the strain in the c-direction when the magnetization is rotated from the basal plane to the c-direction, λ_A is the strain measured in the basal plane, when the magnetization is rotated from the basal plane to the c-direction [89]. Bruno has calculated the relation between the magnetostriction constants and the coefficients of a Néel model [90]. He gives the following expression for the magneto–elastic energy density of the hexagonal system:

$$f_{me}^{hex} = B_1(\alpha_1^2\epsilon_1 + 2\alpha_1\alpha_2\epsilon_6 + \alpha_2^2\epsilon_2) + B_2(1-\alpha_3^2)\epsilon_3 + B_3(1-\alpha_3^2)(\epsilon_1+\epsilon_2) + B_4(\alpha_2\alpha_3\epsilon_4 + \alpha_1\alpha_3\epsilon_5). \tag{3.3}$$

This expression gives the change in the magneto–elastic energy density due to the strains ϵ_i and due to a magnetization along the direction α_i directly, as the demagnetized reference state has already been included. The magneto–elastic coupling coefficients can be calculated from the measured magnetostriction constants and the elastic constants c_{ij} of hcp-Co:

$$\begin{aligned} B_1 &= -(c_{11}-c_{12})(\lambda_A-\lambda_B), & B_2 &= -c_{13}(\lambda_A+\lambda_B) - c_{33}\lambda_C \\ B_3 &= -c_{12}\lambda_A - c_{11}\lambda_B - c_{13}\lambda_C, & B_4 &= c_{44}(\lambda_A+\lambda_B+\lambda_C-4\lambda_D). \end{aligned} \tag{3.4}$$

The values of the magneto–elastic coupling coefficients are given together with the magnetostriction constants in table 2.

In the discussion of magneto–elastic coupling in bulk samples, B and λ are often used synonymously. However, for ferromagnetic films the equivalence between the magneto–elastic coupling and the magnetostrictive strain is not given. In contrast to a bulk ferromagnetic sample, the in-plane strains in a film are fixed due to the strong film–substrate interaction, and cannot freely adjust to minimize the energy of the system. Instead, magnetostrictive *stresses*

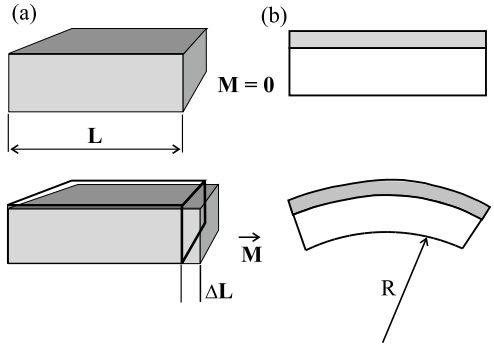

Figure 3. Magneto–elastic coupling in bulk samples and in film–substrate composites. (*a*) The magneto–elastic coupling induces a magnetostrictive strain $\Delta L/L$ in bulk samples. (*b*) The bonding to the substrate induces a magnetostrictive stress that induces a bending of the film–substrate compound. The magneto–elastic coupling coefficient B can be calculated from the radius of curvature R.

are induced in ferromagnetic films. The differences in the magneto–elastic description of bulk samples and ultrathin films films is shown in figure 3.

Therefore, the concept of magnetostriction should be avoided in the description of ferromagnetic films. Instead, the use of magneto–elastic coupling B, which gives the magnetostrictive stress, is preferred. In the following, we briefly compile the expressions for the magneto–elastic coupling in cubic and hexagonal systems. The relations between B and λ are given for completeness.

In the case of ferromagnetic films, that are bonded to a substrate, the above quoted relations between magnetostrictive strain and magneto–elastic coupling coefficients do *not* apply. Whereas the minimization of the elastic and magneto–elastic energy contribution of bulk samples is performed by treating the six strain components as variables to find the minimum of the energy expression, the bonding to the substrate leaves the strain component perpendicular to the film plane as the only variable. The magneto–elastic coupling induces magnetostrictive *stresses* in the film, but the amount of observable magnetostrictive strain in the film plane depends on the experimental conditions, e.g. thickness and rigidity of the substrate. Consequently, only for the strain component ϵ_3 is it meaningful to talk about magnetostrictive strain. The minimization of elastic and magneto–elastic energies gives for a cubic system $\epsilon_3 = -(\epsilon_1 + \epsilon_2)c_{12}/c_{11} - B_1\alpha_3^2/c_{11}$. The change of ϵ_3 due to magnetization along [001], $\alpha_3 = 1$, with an isotropic distribution of the magnetization as a reference state, can be defined as the magnetostriction of films that are clamped to a substrate:

$$\lambda_{100}^{\text{film}} = -\frac{2}{3}\frac{B_1}{c_{11}}. \tag{3.5}$$

Note that due to the bonding to the substrate, c_{12} does not enter this expression [78], in contrast to the discussion of bulk samples above.

3.1. Surface effects and strain dependence of the magneto–elastic coupling in ultrathin films

With decreasing thickness the relative number of film atoms that are bonded at the surface and interface of the film increases. The atomic environment of these interface atoms differs from that of bulk atoms. At the surface, bonding partners are missing, at the interface, bonds are formed between different atomic species. Thus, the symmetry of a surface layer might

differ from the symmetry of the bulk, and additional magneto–elastic coupling coefficients might be necessary to take this so-called surface effect into account. A comprehensive discussion of the magneto–elastic coupling in view of symmetry considerations is presented in [82] and surface contributions to the bulk magneto–elastic coupling coefficients have been defined by Trémolet de Lacheisserie [93]. The bulk and surface magneto–elastic coupling coefficients have been derived in a Néel model [94] of interaction between nearest-neighbour atom pairs [95]. The interaction energy in a Néel model depends on the distance between two atoms and on the orientation of the magnetic moments of the atoms with respect to the vector joining the two atoms. This is a rather crude model for the itinerant magnetism of the 3d-metals, and the outcome of such calculations has to be taken as qualitative result rather than a quantitative prediction, as the authors admit [95]. Based on serious difficulties in applying a Néel model to surface magnetic anisotropies, doubts have been formulated about the applicability of the Néel model to the discussion of anisotropy issues [96]. Fully relativistic calculations do not rely on the conceptual limitations of localized moments and pair interactions and are capable of investigating magnetic anisotropy and magneto–elastic coupling from first principles [12–14, 78, 97, 98]. The implication of these *ab initio* calculations for an atomistic understanding of the relevant processes are briefly discussed in section 3.2.

Experimental evidence for the deviation of magneto–elastic coupling in the surface layer of a ferromagnetic sample was initially presented by Sun and O'Handley [5]. They measured the influence of an externally applied strain on the anisotropy of various amorphous alloys by measuring the spin polarization of secondary electrons. It was found that the magnitude of the magneto–elastic coupling near the surface is more positive and leads to a deviation from the respective bulk values by factors of 2–3. Later, this so-called surface contribution to the magneto–elastic coupling was ascribed to a surface magneto–elastic coefficient B_S. This surface term describes a correction of the bulk magneto–elastic coupling coefficients that is independent of the film thickness t and contributes to the effective magneto–elastic coupling via $B_{\text{eff}} = B_{\text{bulk}} + B_S/t$ [99].

Experimental data on the thickness dependence of the magneto–elastic coupling in ferromagnetic multilayers have been reviewed by Szymczak and Żuberek [6] and Szymczak [7]. Their data are compiled in terms of a surface magnetostriction and reveal a substantial decrease by more than a factor of three of the magnitude of the magnetostriction to more negative values with decreasing film thickness. A linear relation between the magnetostriction and the reciprocal film thickness was found.

Strain is a further important parameter that influences the magnetic anisotropy, as indicated in the linear strain–anisotropy relation of the magneto–elastic energy density above in (3.1). In ultrathin films the misfit between film and substrate is often as high as several per cent and strain-dependent corrections to the magneto–elastic coupling coefficient should be considered [100–102]. The strain correction in its simplest form $B_1^{\text{eff}} = B_1 + D\epsilon$ was successfully applied to account for the stress dependence of the magneto–elastic coupling in epitaxial Fe(100)-films of 100 nm thickness [9] and will be shown to describe the magneto–elastic coupling in epitaxially strained nm Fe-films in section 7. The strain correction to B_1 is found to change the magnitude and sign of the magneto–elastic coupling even for moderate strains in the sub-per cent range. A similar dependence of the magneto–elastic coupling on strain was found in bulk samples. Externally applied stresses in the GPa range have been reported to modify the saturation magnetostriction of amorphous glasses [103, 104].

The role of alloy formation for the magneto–elastic coupling has been studied for CoPd alloys and multilayers [91, 92, 105–108]. The data for the Co-rich CoPd bulk alloy are often used as a reference for the magnetostriction constants of fcc Co, $\lambda_{100}^{\text{fcc Co}} = 120 \times 10^{-6}$ and $\lambda_{111}^{\text{fcc Co}} = -100 \times 10^{-6}$ [91, 92]. The authors find that the magneto–elastic coupling in Co–Pd

multilayers is not governed by the magnetostrictive properties of Co, but by those of the CoPd alloy. They ascribe this effect to the electron hybridization between Co and Pd and to the possibility of alloy formation at the the Co–Pd interface [92, 108].

Finally, a further mechanism that might induce magneto–elastic coupling that deviates from bulk behaviour is the influence of film morphology on the magnitude of the magneto–elastic coupling. Kim and Silva reported an increase of the magnetostriction in ultrathin permalloy films from essentially zero to negative values of order -2×10^{-6} for a film thinner than 7 nm [8]. The deviation from the bulk behaviour was correlated with the measured increase of the surface roughness, although additional influence of residual stress was not excluded.

In conclusion, this discussion of some aspects of the peculiarities of the magneto–elastic coupling in ultrathin films reveals that, in general, a novel magneto–elastic behaviour has to be expected. Physical models that go beyond the simple strain dependence of the magneto–elastic energy density presented in (3.1) and (3.3) are called for and surface magneto–elastic coupling may also become significant relative to bulk magneto–elastic coupling.

3.2. First principles calculations of magneto–elastic coupling

The tiny relative changes of length of bulk Fe, Co, or Ni samples due to magnetization processes of order 10^{-5} indicate that the underlying physical processes are characterized by rather small magneto–elastic energy contributions. To get a rough estimate for the corresponding energy contributions, we recall from section 2 that a strain of 10% leads to an increase of the elastic energy of 0.2 eV/atom. Thus, the four-orders-of-magnitude-smaller magnetostrictive strain can be roughly estimated to change the elastic energy contributions of order 20 μeV/atom. Calculating magneto–elastic effects requires us to determine the total energy of the system with the highest possible precision. Energy changes smaller than μeV/atom have to be traced reliably. The physical reason for the smallness of these effects in the ferromagnetic 3d-elements is that in contrast to the ferromagnetic 4f-elements the orbital moment of the 3d-electrons is almost completely quenched by the crystal field and the spin–orbit interaction removes this quenching only in part, leading to small magnetic anisotropy energies [83]. Nevertheless, a linear strain dependence of the magneto–crystalline anisotropy and the magnetostriction of bulk samples have been determined in recent first principles calculations. Some of this work is briefly discussed in this section to indicate that the phenomenological approach of a strain-dependent contribution to the anisotropy is justified by first principles calculations.

Wu *et al* [12] have calculated the total energy E of bcc Fe, fcc Co, and fcc Ni slabs as a function of the length of the c-axis using the full potential linearized augmented-wave (FLAPW) method. The magneto–crystalline anisotropy energy was calculated from the expectation value of the angular derivative of the spin–orbit coupling with the spin oriented $\theta = 45^\circ$ from the normal axis [109]. Their results are presented in figure 4. This torque method gives the magneto–crystalline anisotropy E_{MCA} as the energy difference between the magnetization oriented in plane, $\theta = 90^\circ$, and out-of-plane, $\theta = 0^\circ$: $E_{\mathrm{MCA}} = E(\theta = 90^\circ) - E(\theta = 0^\circ)$. Thus a positive magneto–crystalline anisotropy energy indicates an easy axis of magnetization that is oriented parallel to the perpendicular c-axis. This dependence of the magnetic anisotropy on the sign of E_{MCA} will be discussed later when the anisotropy of monolayers is discussed.

Figure 4 shows the calculated total energies given by solid circles for bcc Fe (*a*), fcc Co (*b*) and fcc Ni (*c*) on the left axis. The magneto–crystalline anisotropy energy E_{MCA} is given by open circles on the right axis. The data are plotted against the length of the c-axis for a constant volume deformation. The solid curves through the data points of the total energy are parabolic fits to the data. The x-value of the minimum of the parabola indicates the calculated

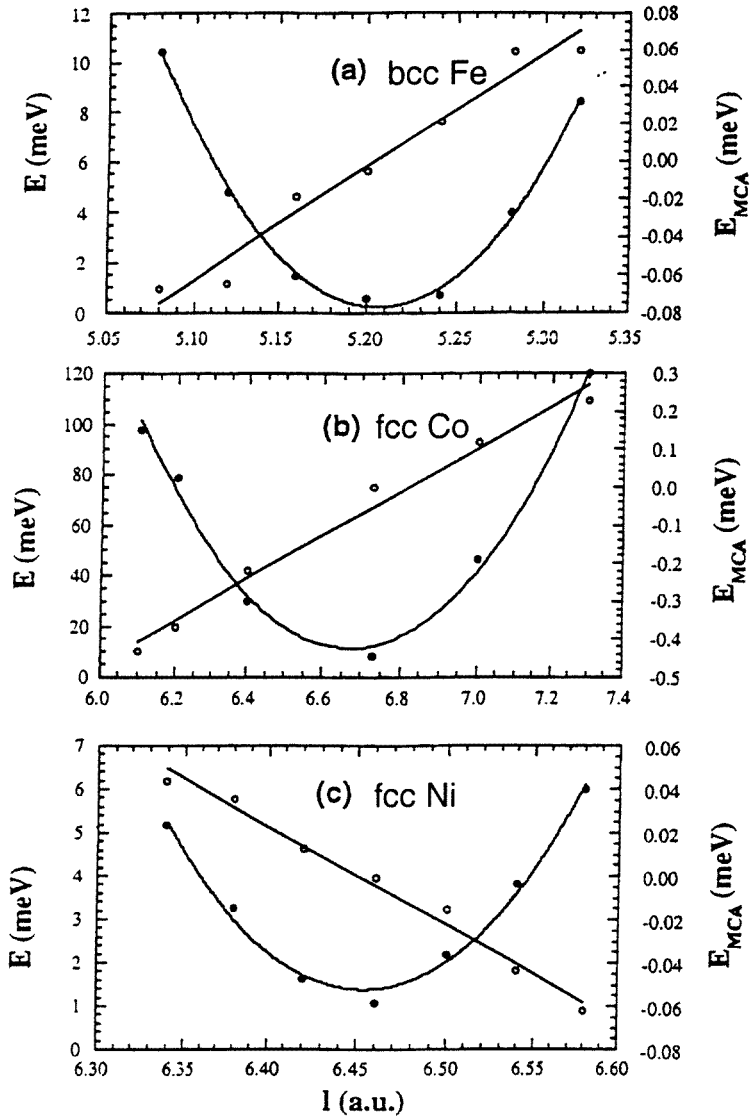

Figure 4. Calculated total energy (left axis, solid circles) and magneto–crystalline anisotropy energy (right axis, open circles), from [12]. The data are plotted for bcc Fe (*a*), fcc Co (*b*) and fcc Ni (*c*) as a function of the length of the *c*-axis. These first-principles calculations indicate a linear dependence of the magneto–crystalline anisotropy on the lattice parameter *l*, as indicated by the straight line through the open data points.

equilibrium lattice constant along the *c*-direction.

For our discussion of magneto–elastic coupling, the most important result presented in figure 4 is the linear dependence of the magneto–crystalline anisotropy energy on the length of the *c*-axis, as indicated by the linear fits to the open data points. Thus, a linear relation,

$$E_{\mathrm{MCA}} = k_1 l + k_2 \tag{3.6}$$

between the magneto–crystalline anisotropy and the length of a lattice parameter l is found in first-principles calculations. The constants k_1, k_2 can be traced back to magneto–elastic

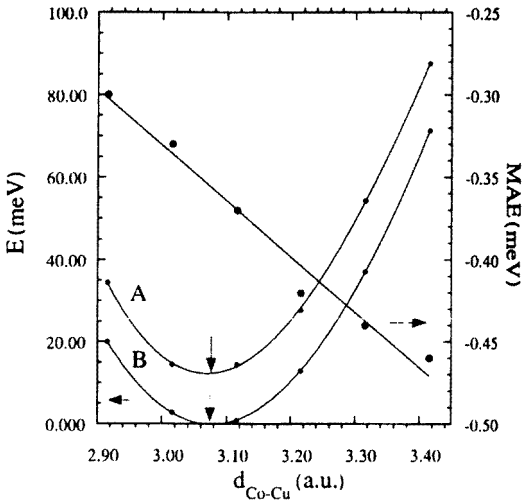

Figure 5. Calculated total energy (left axis) and magnetic anisotropy energy (right axis) of a pseudomorphic Co monolayer on Cu(100), from [78]. The data are plotted as a function of the interlayer distance $d_{\mathrm{Co-Cu}}$. Two parabolic total energy curves (A: scalar-relativistic, B: relativistic for perpendicular spin quantization axis) are presented, a linear dependence of the magnetic anisotropy energy MAE on the perpendicular layer distance is indicated by a linear fit to the data.

coupling coefficients and magneto–crystalline anisotropies, respectively [13, 78]. The authors calculate the magnetostriction constant λ_{100} from the linear fit to the data [12]. The calculated value of λ_{100} of Fe is almost a factor of three larger than the experimental value of 21×10^{-6}, the value for Co, 102×10^{-6}, is within the range of experimental data, the calculated value for Ni is 50% larger than the experimental value of -49×10^{-6}. The authors ascribe the discrepancy between calculated and measured magnetostriction data to the issue of the constant volume distortion mode they adopted.

Qualitatively, the sign of the calculated magnetostriction constant can be extracted from the slope of the magneto–crystalline anisotropy energy as a function of the length of the *c*-axis. A positive slope of this curve in figure 4(*a*) and (*b*) indicates that the energy difference between the in-plane and perpendicular spin orientation, $E(\rightarrow) - E(\uparrow)$, becomes larger for an increase of the *c*-axis length. A perpendicular spin orientation is energetically favourable for the expanded lattice, as indicated by the more positive energy difference, therefore the system will expand upon magnetization along the *c*-axis, as calculated for Fe and Co. A negative slope indicates that a lattice contraction is energetically favourable, as calculated for Ni in figure 4(*c*).

Shick *et al* have calculated the magnetic anisotropy energy and the magneto–elastic coupling of a pseudomorphic Co monolayer on a Cu(100) slab [78]. In contrast to the calculations presented above, now the in-plane lattice constant of the Co monolayer is fixed, while the vertical Co–Cu interlayer distance is varied. Their results on the total energy and the magnetic anisotropy energy of a Co monolayer on Cu(100) are presented in figure 5.

Note, that at the minima of the parabolic energy curves the magnetic anisotropy energy is negative (-0.36 eV), indicating an easy magnetization direction in the film plane. The authors discuss the linear dependence of the magnetic anisotropy energy in view of surface

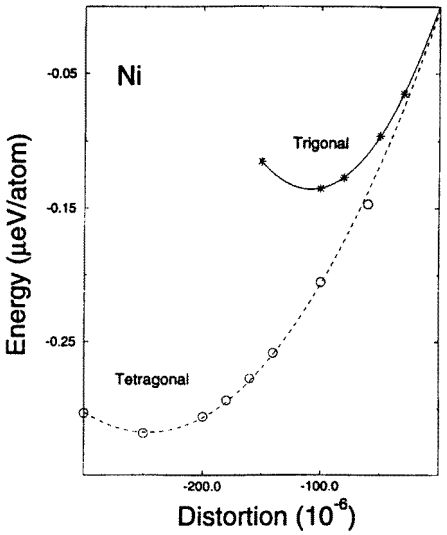

Figure 6. Calculated total energy shift due to small tetragonal and trigonal distortions of Ni, from [13]. The minima of the curves directly indicate the magnitude of the magnetostrictive strains λ_{100} (tetragonal curve) and λ_{111} (trigonal curve). Note the small energy scale.

contribution to both magneto–crystalline anisotropy and magneto–elastic coupling energy,

$$E = -B_1^{\mathrm{V}}(e_\perp - e_0) - \frac{B_1^{\mathrm{S}}}{t}(e_\perp - e_0) + \frac{2K_2}{t}. \tag{3.7}$$

Here, the difference between the out-of-plane and in-plane strain, $e_\perp - e_0$, is defined with respect to the bulk lattice constant of fcc Co of $a_{\mathrm{fcc\ Co}} = 3.55$ Å. The volume magneto–elastic coupling B_1^{V} was calculated from λ_{100} of a Co-rich PdCo alloy [91], $2K_2$ was obtained from figure 5 as -0.47 meV per atom where $(e_\perp - e_0) = 0$. Thus, the surface magneto–elastic coupling coefficient B_1^{S} was calculated from the difference between the total and the volume magneto–elastic energy. It was pointed out by the authors that these results resemble a qualitative similarity between first-principles theory and the Néel model [78].

Hjortstam *et al* [13] calculated the magnetic anisotropy in tetragonal distorted Ni for constant area and constant volume distortions. They found for both types of distortions a linear dependence of the volume anisotropy K_V on the tetragonal distortions given by the ratio of the out-of-plane lattice and in-plane constants c/a. Again, the magnetic anisotropy energy is defined as the difference of the total energy between an in-plane orientation of the magnetization and an out-of-plane orientation of the magnetization, $K_V = E(\rightarrow) - E(\uparrow)$. They ascribe the linear dependence of K_V on the c/a-ratio to the magneto–elastic coupling [13]:

$$K_V = \tfrac{3}{2}\lambda_{100}(c_{11} - c_{12})(\epsilon_2 - \epsilon_1). \tag{3.8}$$

Here, the magnetostriction constant λ_{100} and the elastic constants c_{11}, c_{12} of Ni are used to characterize the magneto–elastic coupling. The in-plane strain of the lattice parameter a is given by ϵ_1, ϵ_2 describes the strain along the perpendicular direction with lattice parameter c. The authors calculated c_{11} and c_{12} previously [110] and are therefore in the position to calculate λ_{100} from their value of K_V at a given strain. Note, that the prefactor in front of the strain difference $\epsilon_2 - \epsilon_1$ can equally be written as $-B_1$, see (3.2). The calculated value of λ_{100} is more than a factor of three larger than the experimental value. This deviation between theory and experiment is ascribed to the smallness of the underlying energy changes [13].

In addition, they *directly* calculated the shift of the total energy of Ni due to extremely small distortions of order 10^{-4} [13]. The result is presented in figure 6. The minima of the curves directly indicate the magnitude of the magnetostriction constants λ_{100}, obtained from a

tetragonal lattice distortions, and of λ_{111}, obtained from trigonal lattice distortions. Note that in contrast to the calculations presented above, the x-scale is as small as the magnetostrictive strains. Due to the smallness of the distortions, the resulting energy changes are only of the order of several neV per atom. Clearly, an astonishing numerical accuracy is required to perform these calculations. The calculated magnetostrictive strains are a factor of three larger than the experimental values. But nevertheless, a direct calculation of magneto–elastic effects seems feasible.

Finally, the close relationship between the electronic structure and the magnetic interface anisotropy has been studied in first principles calculations [97, 111–116]. The band filling was recognized as an important parameter that determines the magnetic anisotropy of Co/Ni and Co/Pd multilayers [112] and of free-standing Fe [114] and Co monolayers [117]. Kyuno *et al* have performed first principles calculations on the magneto–elastic anisotropy of fcc Pd/Co multilayers, unsupported Co monolayers, and bulk fcc Co [98]. They suggest that a large local density of states of $\mid m \mid = 2$ character, as they found for Pd/Co multilayers, favours a perpendicular easy axis of magnetization, in agreement with experimental results [45].

Recent theoretical investigations offer an electronic picture of the origin of the strain dependence of the magnetic anisotropy [12, 109]. The hybridization of the d states of the ferromagnetic material with the substrate has been identified to be the main driving force for the magnetostriction along the film normal in fcc Co(100) monolayers on Cu and Pd substrates. The effects of strain and interdiffusion on the magnetic anisotropy of Cu/Ni/Cu(001) sandwiches has been studied in first-principle calculations [14]. These theoretical investigations all indicate the key role of hybridization between electronic states to account for the magnetic anisotropy and its strain dependence.

In conclusion, one has to be aware of the limitations of simple phenomenological models presented above, in the discussion of magnetic anisotropy and magneto–elastic coupling in monolayers. First-principle theory suggests that there is more to magneto–elastic coupling than a mere strain dependence of the anisotropy energy. In general, the magneto–elastic coupling in monolayers should also depend on the nature of the substrate atoms, and not only on the strain in the film.

4. Experimental techniques to investigate magneto–elastic coupling

Various techniques that can be used to determine the magneto–elastic coupling in bulk samples and in ferromagnetic films are discussed in the books by Bozorth [1], du Trémolet de Lacheisserie [82] and in the review article by Lachowicz and Szymczak [118]. We briefly compile direct and indirect methods that have been applied in the study of magneto–elastic effects and conclude with a more comprehensive analysis of the venerable bending beam technique that allows us to measure both magneto–elastic coupling *and* film stress in one experiment.

For bulk samples strain gauge techniques have been used to measure the change in length of the sample during a magnetization process. From the relative change of length measured along a certain direction for magnetization along another direction all magnetostriction constants of cubic and hexagonal systems have been determined, and procedures for the appropriate orientation of the sample plane, the measuring direction and the magnetization direction are given in the literature [84–89, 119, 120].

Alternatively, the bulk sample can be made part of a plate capacitor, and magnetostrictive changes of the sample length can be measured with high sensitivity by monitoring the resulting change in capacity of the set-up. To achieve ultimate sensitivity and to keep the influence of stray capacities low, a three-terminal capacitor method is used [121–123]. Even the smallest

magnetostrictive strains of *paramagnetic* transition metals of order 10^{-10} have been measured for cm-long samples [122].

The magnetostrictive strain of bulk samples has been measured with fibre-optic techniques [124, 125]. The sample has been used as a shutter in a fibre-optic path of light. Thus a periodic magnetostrictive strain modulated the light intensity [126]. The distance between the end of an optic fibre and the magnetostrictive sample was measured with an interferometric technique, the reported sensitivity was 10^{-6} for a cm-long sample [127]. The dependence of a tunnel current between a tunnelling tip and a magnetostrictive sample on the distance between tip and sample has been used to measure magnetostriction in a feedback-loop mode of operation [128, 129]. However, the tunnelling experiment is extremely susceptible to vibrational and electronic noise and did *not* exceed the sensitivity of capacitance or optical interferometric techniques [128].

For bulk samples in the form of ribbons and wires the *Wiedemann effect* has been shown to allow a very accurate determination of the saturation magnetostriction of elastically and magnetically isotropic samples [82]. The basic idea of the Wiedemann effect is to measure the torsion that is induced in a wire when the wire is magnetized along its length by an external field and a current is run along the axis of the wire. The current induces a circular magnetic field, oriented perpendicular to the wire axis. The magnetization of the wire will be deflected by the effective magnetic field. A magnetostrictive strain is induced in the cross section of the wire, and the wire will twist [82]. Pidgeon has measured the torsion of Ni and Co wires as a function of the longitudinal field and for different currents through the wires to determine the magnetostriction constants of polycrystalline Ni and Co as early as 1919 [130]. The same effect was used to measure the torsional magnetostrictive strain in amorphous metal ribbons [131] and with a high sensitivity of 10^{-13} in thin-walled Ni tubes [132].

These direct methods directly evaluate the magnetostrictive strain or the magnetostrictive torsion to determine the magnetostriction constants. In the following indirect methods the samples are exposed to an externally applied stress by pressing, stretching or bending the samples. The effect of this externally imposed strain of the sample on the magnetic properties like initial susceptibility, the shape of the magnetization curve, or the ferromagnetic resonance is analysed to derive the magneto–elastic coupling coefficients. The main idea of these indirect methods is to exploit the contribution of the magneto–elastic coupling as described in (3.1) to the magnetic anisotropy. Straining the sample will change the effective anisotropy due to the magneto–elastic coupling.

The effect of tensile stresses on the initial susceptibility of amorphous alloys has been investigated to derive the saturation magnetostriction constant [103, 133–135]. In these experiments the measured proportionality between the reciprocal initial susceptibility and the applied stress is analysed to derive the magnetostriction constant. The simple idea behind these experiments is that the anisotropy of these amorphous alloys is mainly due to the magneto–elastic coupling. Thus, straining ($\epsilon > 0$) an amorphous sample with a negative magnetostriction constant will increase the effective anisotropy and lower the initial susceptibility. The appearance of the whole magnetization curve is affected by the strain that one imposes on the sample [5, 102, 136, 137]. Thus, in general, the measurement of the magnetization curve can be analysed to calculate the effective magneto–elastic coupling of the sample from the effect of strain on the initial susceptibility, or on the effective anisotropy. However, certain models of what contributes to the effective anisotropy are needed.

The contribution of the magneto–elastic anisotropy to the effective anisotropy of amorphous samples can also be probed in the small-angle magnetization–rotation (SAMR) method. Here, a constant magnetic field acts along the axis of a ferromagnetic film or wire, while a smaller perpendicular ac-magnetic field tries to deflect the magnetization direction by a small amount of order 1° away from the axis. The deflection of the magnetization direction is

usually detected inductively by a pick-up coil with a lock-in amplifier. The signal of the sense coil is measured for different externally applied stresses imposed on the sample by stretching the ferromagnetic wire [138, 139], ribbon [103, 140], or film–substrate composite [141, 142].

Finally, the ferromagnetic resonance (FMR) method [43] can be used to determine the magneto–elastic properties of ferromagnetic samples. The idea of these measurements is to measure the shift in the resonance field as a function of the externally applied stress to a bulk samples [143, 144]. This method has been applied to 640 nm thick polycrystalline Ni films by measuring the shift in the resonance field while bending the film–substrate composite [145]. The authors claim that the shift of the resonance field has to be measured with a sensitivity of 10^{-6} T to achieve a sensitivity of 10^{-7} for the determination of the magnetostriction constants. A method for determining both magnetostriction and elastic modulus of μm Ni films by FMR has been described for a triangular polymer beam as a substrate [146]. A related technique is Brillouin-light-scattering (BLS) [147, 148]. The shift in frequency of visible light due to inelastic scattering at spin-waves is measured with ultrahigh resolution spectrometers. The analysis of the spectra allows to determine all magnetic anisotropy contributions in ultrathin films [50].

5. Stress measurements with cantilevered substrates

Experimental techniques that measure film stress *directly* exploit the bending moment that is exerted by the film stress onto the substrate. Measurements of film stress therefore usually rely on an analysis of the substrate curvature that results from the bending moments due to film stress. The film stress can be caused, for example, by epitaxial misfit between film and substrate [149–152], solid-state reactions between film and substrate [153], ion implantation [154], or by the magneto–elastic coupling in a ferromagnetic film during a magnetization process [82, 155–159]. The magnetostrictive bending of a highly magnetostrictive Terfenol-D film deposited on a μm thin Si microcantilever has been proposed as a magnetometer [160]. The intrinsic stress of polycrystalline films has been reviewed by Doerner and Nix [161], Abermann [162], Koch [163], and for epitaxial films by Koch [152]. The mechanical properties of thin films have been discussed by Hoffman [164], Kinosita [165] and Nix [166, 167]. The relaxation of intrinsic film stress during heat treatments was investigated by measuring the change of radius of curvature of the film–substrate composite with scanning and multiple beam optical techniques [168, 169]. The contribution of surface and interface stress effects to the stress-induced bending during film and multilayer growth was analysed with optical deflection techniques [170, 171]. In addition, changes of the surface stress of the substrate due to adsorption [172–175], surface reactions [176], film growth [177–180] or surface reconstruction [181–183] can be monitored with sub-monolayer sensitivity [21].

The cantilevered substrate–film composite can be used as a magnetometer, as an external deflecting field B acting on the total magnetic moment of the film m_{total} gives rise to a torque $\vec{T} = \vec{B} \times \vec{m}_{\text{total}}$ [184–187]. If the film magnetization is oriented along the sample length (or perpendicular to the film plane) and the deflecting field is perpendicular to the film plane (along the sample length), the resulting torque induces a bending of the substrate. Miniaturized versions of torque magnetometers have been described recently as very sensitive magnetic field sensors [188] and for capacitive torque magnetometry [189]. A measurement of the field-induced substrate curvature gives the total magnetic moment of the film directly in absolute units. The quantitative results of the bending beam magnetometry is superior to the commonly used magneto-optic Kerr-effect (MOKE) measurements [190, 191], that give only a signal proportional to the magnetization of the sample. However, rather stringent requirements apply to the proper orientation between the deflecting field and direction of magnetization to make

the beam magnetometer work. In contrast to MOKE, at least one additional set of magnets is necessary to produce the deflecting field with the proper orientation.

Film stress *and* magneto–elastic coupling has been measured *in situ* by monitoring the substrate curvature during film growth and during magnetization processes [9, 10, 184–187, 192–194]. These combined measurements on film stress and magneto–elastic coupling reveal the important role of film stress for the modified magneto–elastic coupling in strained films. A discussion of this topic follows in section 7.

5.1. Film stress-induced substrate bending

A rigorous treatment of the substrate curvature based on elastic energy considerations has been given by Marcus [195] and Ibach [21]. Fukuda has solved the differential equations of elasticity to discuss the bending of 300 mm Si wafers during thermal treatment [196, 197]. We present a physical transparent derivation of the curvature analysis that is based on the discussion of two-dimensional curvatures of thin plates as worked out, for example, by Timoshenko and Woinowsky-Krieger [198].

It has to be kept in mind that for applications of interest in this review, the film thickness t_F is smaller than 100 nm and amounts to maximal 0.1% of the substrate thickness t_S, that is usually of order 100 μm. Secondly, the minute forces that act in the film lead to very small changes of the curvature of the substrate. Typically, the radius of curvature R of the substrate is of order 100 m for epitaxial misfit-induced film stress or even orders of magnitude larger in the case of magnetostrictive bending. Thus, the end of a 10 mm long substrate will be deflected by only 500 nm when the substrate is curved with a radius of curvature of 100 m. The deflection of the end of the substrate amounts to less than 1% of the substrate thickness and the approximations of the theory of small deflections of thin plates [198] are assumed to apply. For the derivation of the film stress from a measurement of the curvature of the substrate we can safely consider the film stress to be constant through the film thickness, and no appreciable stress relaxation occurs due to the bending. Note that a radius of curvature of $R = 100$ m induces only a negligible strain on the substrate surface of less than 10^{-6} for $t_S = 100$ μm. An appreciable stress relief in the films becomes important for $t_F/t_S > 0.01$, as shown by Röll [199].

A stress acting in the surface or in a film tends to bend the substrate *and* tends to compress or dilate the substrate. Both effects can be treated separately, as proposed by Brenner and Senderoff [200] and by von Preissig [201], according to the schematic presented in figure 7. Imagine a film stress $\tau_F = F/A_F$, (A_F: cross section of the film), acting on the surface of the substrate, figure 7(*a*). The straining action of the stress will cause the substrate to change its length, as indicated in figure 7(*b*). The bending moment of the film stress is given by $F \times r$, figure 7(*c*). The bending moments induce a biaxial curvature and the strain of the substrate ϵ_S changes through the substrate thickness t_S, figure 7(*d*). The superposition of the straining and bending effects presented in figure 7(*e*) reveals that the neutral axis moves away from the middle of the substrate. A detailed calculation of the force and moment equilibrium shows that the neutral layer shifts $\frac{2}{3}$ of the substrate thickness away from the stress loaded surface [200]. This separation of the straining and bending effects is very beneficial, as the curvature–stress relations for biaxial stress can be deduced very easily for substrates with isotropic elastic properties, like W. Most crystalline substrates however, are highly anisotropic. The directional dependence of Young's modulus Y and of Poisson's ratio ν has to be considered as discussed in section 2. The following expressions hold for cubic (100) and (111) and for hexagonal (0001) substrate orientations, provided that Y and ν are inserted for the respective orientation.

The relations between the biaxial bending moments M_x and M_y and the radii of curvature

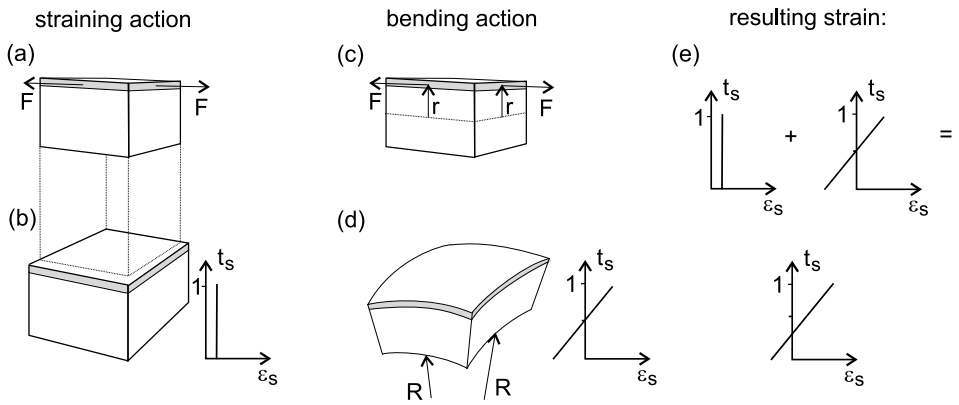

Figure 7. Stress-induced substrate curvature. The stresses acting in the grey-shaded film give rise to a film force F that induces a straining action (*a*)–(*b*) *and* a bending action (*c*)–(*d*). The resulting substrate strain ϵ_S is sketched as a function of the substrate thickness t_S in (*e*).

R_x and R_y are taken from the theory of plates [198]:

$$\begin{aligned}\frac{M_x}{w} &= \frac{Y_S t_S^3}{12(1-\nu_S^2)}\left(\frac{1}{R_x}+\nu_S\frac{1}{R_y}\right)\\ \frac{M_y}{l} &= \frac{Y_S t_S^3}{12(1-\nu_S^2)}\left(\frac{1}{R_y}+\nu_S\frac{1}{R_x}\right).\end{aligned} \tag{5.1}$$

The width and the length of the substrate are given by w and l, respectively. The subscript S denotes substrate properties, the substrate length is oriented along the x-axis, the width along the y-axis. The bending moments M are given by the film stresses τ. Performing the separation of the bending and straining action of the film stresses, the bending moments are simply given by $M_x = \tau_x w t_F t_S/2$ and $M_y = \tau_y l t_F t_S/2$, and the expressions for the biaxial film stress as a function of the radii of curvature follow as:

$$\begin{aligned}\tau_x &= \frac{Y_S t_S^2}{6(1-\nu_S^2)t_F}\left(\frac{1}{R_x}+\nu_S\frac{1}{R_y}\right)\\ \tau_y &= \frac{Y_S t_S^2}{6(1-\nu_S^2)t_F}\left(\frac{1}{R_y}+\nu_S\frac{1}{R_x}\right).\end{aligned} \tag{5.2}$$

Equation (5.2) gives the in-plane stress components τ_x and τ_y as a function of the experimentally determined radii of curvatures R_x and R_y, measured along *two* directions on a substrate with isotropic elastic properties. Note, that the elastic properties of the film do *not* enter the expressions as we assumed a very small thickness ratio t_F/t_S. In general, two curvatures need to be determined to derive the in-plane stress of a film. However, if the stress is isotropic, $\tau_x = \tau_y$, the well known modified Stoney relation follows $\tau = Y_S t_S^2/(6(1-\nu_S)Rt_F)$. Stoney did not consider the two-dimensional character of the bending problem when he analysed the bending of a 0.3 mm thin steel ruler due to the electrodeposition of μm Ni films and his result did not show the $(1-\nu_S)$ in the denominator [202]. Thus, for isotropic stress acting on an elastically isotropic substrate one measurement of the radius of curvature suffices to determine the film stress τ.

Using the modified Stoney equation and the elastic properties of a W(100) substrate given in table 1, it follows that even a strong epitaxial stress of 10 GPa in a 0.5 nm thin film induces only a minute bending with a large radius of curvature of order 200 m for a 0.1 mm thin W

substrate. Thus, the resulting bending is really very small, and the approximations for small deflections of thin plates do apply.

The application of (5.2) requires a free two-dimensional bending of the substrate. In most cases however, the substrate is clamped along the width to a sample manipulator and the bending is suppressed along the width of the sample near the clamping. In the case of a small length-to-width ratio of a clamped sample, the resulting curvature is almost one-dimensional and can be described by setting $R_y = \infty$ in (5.2):

$$\tau_x^{(1\ \mathrm{dim.})} = \frac{Y_S t_S^2}{6(1-\nu_S^2)t_F}\frac{1}{R_x}. \tag{5.3}$$

Equation (5.3) is easily extended to crystalline substrates that have anisotropic elastic properties. One has to calculate Y_S for a direction along the sample length, and ν_S for the direction along the sample width, as derived in section 2.

Ibach performed experiments to derive the dimensionality of the bending for isotropic substrates with different length-to-width ratios under isotropic stress [21]. Watts *et al* performed finite-element modelling of the issue of clamping for anisotropic magnetostrictive stress [203]. Both works show that already for a length-to-width ratio of two, the error in the calculated stress is only of order 5% when the formulae for free two-dimensional bending are applied to a sample that is clamped at one end. This error gives rise to a small uncertainty in the determination of the *absolute* stress value, but it does not influence the comparability of results obtained for the same length-to-width ratio. However, it is certainly important to quote the the length-to-width ratio and the dimensions of the deposited film to facilitate a comparison between the data obtained under different experimental conditions. In conclusion, for length-to-width ratios larger than two, no detrimental error is expected from the application of the formulae for two-dimensional bending, even for clamped substrates.

5.2. Magneto–elastic coupling and magnetostrictive bending

Although the measurement of magnetostrictive bending has a long tradition since the early work by Klokholm [155], the *evaluation* of the curvature data to obtain the magnetostriction constants has been subject of series of publications [93, 158, 204–209] due to the erroneous formulae used in the early work. The magnetostrictive bending has been analysed in these works by energy minimization procedures or by a detailed treatment of the force and moment equilibrium condition. In the following, we extend the bending moment approach to the analysis of the magnetostrictive induced curvature of a film–substrate composite. In contrast to most of the papers cited above, we make explicit use of the concept of *magnetostrictive stress*. Thus, we derive the relations between the curvature and the *magneto–elastic coupling* without having to deal with the misleading term magnetostriction that does not apply to films that are bonded to a substrate, for reasons given in section 3.

The magneto–elastic coupling in ferromagnetic films gives rise to a change of the energy density of the film that depends on the orientation of the film magnetization with respect to the crystal axis. In contrast to the magneto–crystalline anisotropy, this magneto–elastic anisotropy depends also on the film strain. A magnetization of a cubic film along its x-axis gives rise to an energy contribution of $B_1\epsilon_1$, see (3.1). The film might be strained due to epitaxial misfit, and ϵ_1 can be considered as the misfit strain, which depends on the epitaxial growth and may be as large as 10–20%. This strain remains essentially unchanged during the magnetization process, as the film is rigidly bonded to the substrate, and the radius of curvature of the substrate is so large, that no appreciable strain relaxation occurs. It is assumed for the moment, that the magneto–elastic coupling coefficients B_i are constants and do not depend on the film strain. As

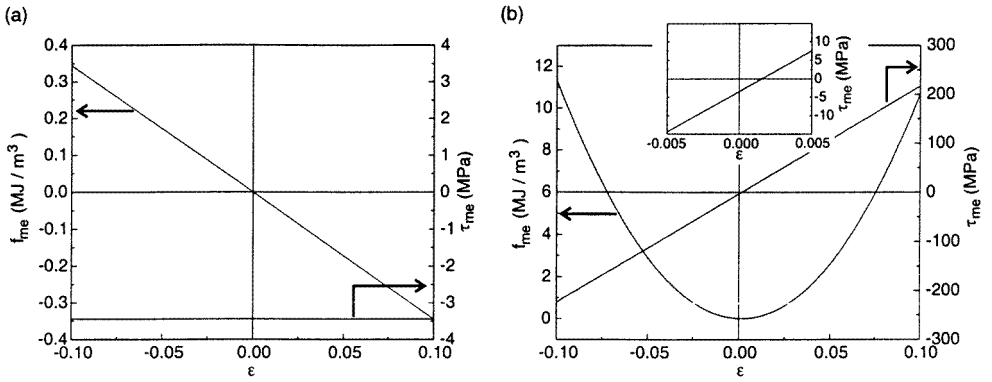

Figure 8. The magneto–elastic energy density f_{me} (left axes) and the magnetostrictive stress $\tau_{me} = \partial f_{me}/\partial\epsilon$ (right axes) for (*a*) $f_{me} = B_1\epsilon$, and (*b*) $f_{me} = B_1\epsilon + D\epsilon^2$. Plotted for Fe: $B_1 = -3.44$ MJ m^{-3}, $D = 1100$ MJ m^{-3} [9, 194]. Note that a constant magnetostrictive stress results in (*a*), whereas in (*b*), the magnetostrictive stress is zero for $\epsilon = 0.0016$ (inset (*b*)).

we shall see later, this assumption is not necessarily justified for strained films and, in general, one has to take the strain dependence of the B_i into account. This can be done by introducing an effective magneto–elastic coupling $B_1^{\text{eff}} = B_1 + D\epsilon_1$ [9, 100]. The important point is that the magneto–elastic coupling leads automatically to magnetostrictive stresses that are given by the strain derivative of the magneto–elastic energy density.

The relation between magneto–elastic energy density and magnetostrictive stress is illustrated in figure 8. The negative $B_1 = -3.4$ MJ m^{-3} of bulk Fe leads to a lower magneto–elastic energy density for positive strains, as indicated by the negative slope of figure 8(*a*). Bulk Fe can lower its energy by expanding upon magnetization, as known from its positive $\lambda_{100} = 24 \times 10^{-6}$. Alternatively, one can describe this tendency to expand upon magnetization with a compressive stress, indicated by $\tau_1 = \partial f_{me}/\partial\epsilon = B_1 = -3.4$ MPa, and plotted on the right axes of figure 8. This magnetostrictive stress is compensated by the elastic stress $\tau^{\text{elastic}} = -B_1$ and the magnetostrictive strain follows directly $\epsilon_1 = -s_{11}B_1 = -B_1(c_{11}+c_{12})/((c_{11}-c_{12})(c_{11}+2c_{12}))$ in agreement with the energy minimization calculations [2, 11]. The expression for s_{11} was taken from the appendix. In its simplest form, $f_{me} = B_1\epsilon$ the magneto–elastic energy density leads to a constant magnetostrictive stress, no matter how large the initial strain is. Taking the strain dependence of B_1^{eff} into account, a quadratic dependence of the magneto–elastic energy density on the film strain results, figure 8(*b*). It follows that the magnetostrictive stress is now a linear function of the film strain, and there is *no* magnetostrictive stress at the zero crossing of the stress curve in the inset of figure 8(*b*). A ferromagnetic film with that peculiar strain will not induce any magnetostrictive stress, as if the magneto–elastic coupling was zero. Such a zero crossing of the magnetostrictive stress was observed and is discussed below.

If the film magnetization direction is switched from parallel to the sample length to parallel to the sample width, the magnetostrictive stress changes its orientation accordingly. An anticlastic curvature results as a magnetostrictive stress is induced exclusively along the magnetization direction. From (5.2) it follows that $R_y = -R_x/v$ for the stress $\tau_y = 0$ for a magnetization along the x-direction. A biaxial curvature with opposite signs of the radii of curvature results. The substrate is bent to a saddle-like surface.

In most experimental situations the resulting changes in curvature is observed along the

sample length in the x-direction and from (5.2):

$$\Delta\tau_x = \frac{Y_S t_S^2}{6(1-\nu_S^2)t_F}\left(\left(\frac{1}{R_x}\right)^{\text{length}} + \nu_S\left(\frac{1}{R_y}\right)^{\text{length}} - \left(\frac{1}{R_x}\right)^{\text{width}} - \nu_S\left(\frac{1}{R_y}\right)^{\text{width}}\right). \tag{5.4}$$

Here, the superscripts *length* and *width* describe the direction of magnetization. The magnetostrictive stresses are equal for magnetization along the length and along the width. The curvatures for saturation magnetization along the length and width are identical, $R_x^{\text{length}} = R_y^{\text{width}}$ for an isotropic elastic substrate, and the same holds for the perpendicular curvatures $R_x^{\text{width}} = R_y^{\text{length}}$. Some simplification of (5.4) is possible, and the final result is:

$$B_1 = \frac{Y_S t_S^2}{6(1+\nu_S)t_F}\left(\left(\frac{1}{R_x}\right)^{\text{length}} - \left(\frac{1}{R_x}\right)^{\text{width}}\right). \tag{5.5}$$

A compressive magnetostrictive stress, $B_1 < 0$, induces a negative curvature for this choice of the coordinate system. The magneto–elastic coupling coefficient B_1 for cubic film can be determined by measuring the change of radius of curvature of the film substrate composite that results when the magnetization is switched from the direction along the sample length to the sample width. The elastic properties Y_S, ν_S have to be calculated for the surface orientation, and (5.5) holds for substrate surfaces with an at least threefold rotational symmetry around the surface normal. Again, the approximations of small deflections of thin plates are assumed to apply. Consequently, the so-called pole effect that leads to an apparent increase of the flexural rigidity of the sample by the formation of magnetic poles at the surface of the film for strong curvatures with large deflections [158, 210] can be neglected for the small deflections that are of interest here.

Equation (5.5) is the same result that is obtained by more rigorous and lengthy energy minimization procedures [158, 209]. Previously, the result has been expressed in terms of λ and the elastic properties of the film [158, 187, 209]. Note, that for the special case considered here, $Y_F/((1+\nu_F)(c_{11}^F - c_{12}^F)) = 1$ and the different notations are seen to be equivalent with $B_1 = -\frac{3}{2}\lambda_{100}(c_{11} - c_{12})$, see (3.2).

6. Stress-driven structural changes and their impact on magnetism

To investigate the intimate relation between film stress, stress-induced structural changes, and magnetism it is very advantageous to measure both film stress *and* magnetic properties *in situ*. The combination of the cantilevered substrate to measure film stress during growth with the magneto-optic Kerr effect (MOKE) [190, 191] reveals the correlation between stress and magnetism with sub-monolayer sensitivity [186].

We use a simple optical deflection technique, sketched in figure 9(*a*), to measure the stress-induced bending of our $\approx$100 μm thin single-crystal substrates. The laser and the position sensitive detector, a split photodiode, are mounted on a platform that is rigidly connected to the atmospheric side of a window flange of the ultra-high vacuum (UHV) chamber. The laser light is reflected from the substrate surface through the window onto the split photodiode. Any change of the radius of curvature of the sample leads to a deflection of the reflected beam that is detected with high sensitivity by the resulting asymmetry of the photo currents between the two parts of the diode [153]. Two optical deflection set-ups are used. One is mounted at the film preparation part of our UHV chamber to measure film stress during film growth and another one, attached to a window at the lower magnetism part of the vacuum chamber shown in figure 9(*b*), measures changes of the substrate curvature during magnetization processes to determine the magneto–elastic coupling coefficients [186]. The schematic cross section of the lower part of

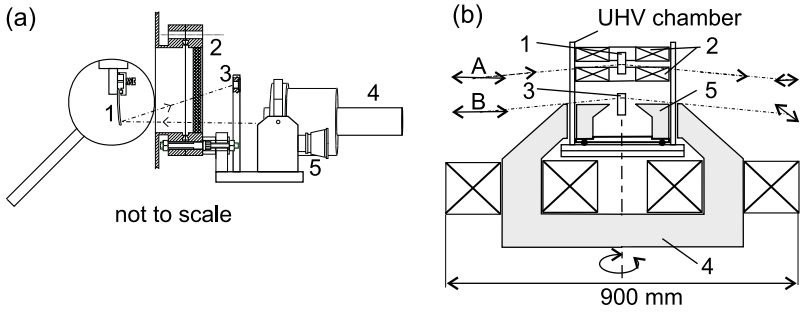

Figure 9. (*a*) Schematic of the optical deflection set-up. 1: sample, 2: UHV window, 3: position sensitive detector on a piezo-electric translator, 4: laser, 5: platform with gimbal mount for convenient laser alignement. After [211]. (*b*) Cross section through the magnetism part of the UHV chamber. The sample can be positioned at 1 in a vertical magnetic field of up to 0.1 T produced by an internal electromagnet 2, while the magnetization is checked with the transversal Kerr effect (light path A). In position 3, the external magnet 4 is used for in-plane and out-of-plane magnetization in fields of up to 0.4 T. Internal pole pieces 5 direct the magnetic flux towards the sample. Longitudinal and polar Kerr-effect measurements are performed (light path B). After [186].

the vacuum chamber in figure 9(*b*) shows two sets of magnets that are employed to magnetize the sample. A large external electromagnet produces fields of up to 0.4 T along the sample width and an *in situ* stainless-steel capsuled and water cooled magnet produces fields of up to 0.1 T along the sample length. The external magnet is mounted on a turntable and can be rotated together with its UHV pole pieces for an out-of-plane magnetization. The magnetization of the film is checked by transversal, longitudinal and polar Kerr-effect measurements. The magnetization-induced bending of the film–substrate composite is measured simultaneously with the Kerr-effect measurements.

In the following, the role of film stress for the high coercivity measured in sesquilayers of Fe on W(110) is discussed before the modified magneto–elastic coupling in nm epitaxial Fe films is analysed in view of strain-induced corrections of B_1 in section 7.

The high sensitivity of optical deflection techniques [211–214] allows us to measure the minute bending with a radius of curvature of order 200 km induced by the magnetization of three Fe monolayers on a 100 μm thick W substrate [215]. Thus, in addition to the correlation between film stress and coercivity [151], the important role of stress for the modified magneto–elastic coupling in monolayers can be investigated *directly* [9, 179, 187, 194]. These measurements on the magneto–elastic coupling in nm thin epitaxial Fe films show that the magnitude and sign of B_1 deviates from the respective bulk value. The *in situ* correlation of these measurements with the film stress indicates a strain-dependent correction of the magneto–elastic coupling coefficient B_1. The following results on film stress and magnetism of Fe monolayers on W(110) and on W(100) were obtained in one ultra-high vacuum chamber that combined stress measurement capabilities with various electromagnets for MOKE and magnetostrictive bending experiments [186].

6.1. Stress and stress relaxations of Fe monolayers on W(110) and their impact on magnetism

The magnetism of Fe monolayers on W(110) was studied intensively in the past [37] and is characterized by a pronounced in-plane anisotropy with an easy axis of magnetization along [110] for an Fe thickness of up to 100 Å [216]. In thicker films, the easy axis of magnetization reverts to [001] as found in bulk Fe. The magnetic properties of Fe monolayers on W(110)

show a peculiar behaviour in the so-called sesquilayer coverage region where one-and-a-half monolayers (ML) cover the W substrate. Initially, a gap of ferromagnetic order was reported for coverages between 1.2 and 1.47 ML [217]. The loss of ferromagnetic order was ascribed to an antiferromagnetic coupling between double-layer islands. Later, a nanoscale spatial switching of magnetic anisotropy between the in-plane in the monolayer region, and perpendicular in the double-layer region was proposed [218, 219]. The perpendicular easy axis of magnetization of the double-layer islands was proposed to be of magneto–elastic origin [218]. In other experiments [151, 220] a high coercivity was found in the sesquilayer region that was ascribed mainly to the pinning of the domain wall movement at the second-layer islands, with a small contribution to the coercivity arising from the stress variation in the film, that will be discussed in some detail below.

The magnetic behaviour of sesquilayer Fe films at a coverage of 1.5 ML, that consist of nm size patches of the second Fe layer on top of the underlying first Fe layer, seems to be extremely susceptible to the structural and morphological properties of the film. Therefore, a detailed analysis of the film stress in the sesquilayer region is presented. The large lattice mismatch $\eta = (a_W - a_{Fe})/a_{Fe} = 0.104$, ($a_W = 3.165$ Å, $a_{Fe} = 2.866$ Å [62]), leads to a tremendous epitaxial strain of more than 10% in the first layer of Fe that grows pseudomorphically. Low-energy electron diffraction (LEED) [221, 222] and photoelectron diffraction experiments [223] reveal that the Fe atoms of the first layer grow in positions that continue the bcc(110) bulk structure of the W substrate in spite of the large lattice mismatch. Assuming the validity of continuum elasticity even in the monolayer range, the resulting epitaxial stress in the Fe film can be calculated as described in section 2. We recall that a tremendous anisotropic film stress of $\tau_{\bar{1}10} = 38.9$ GPa and $\tau_{001} = 27.5$ GPa which leads to a high strain energy per Fe atom in the pseudomorphic layer of 0.32 eV/atom. Thus, stress-induced structural changes can be expected and were analysed in stress measurements during film growth [151, 179, 186]. The beginning formation of misfit distortions already in the second layer of Fe was found to contribute to the high coercivity of sesquilayer Fe films [151].

Remember from (5.2) that the radii of curvature have to be measured along two directions to determine the biaxial stress components. Biaxial stress measurements were performed on two W(110) crystals that were cut with their long edge oriented along the W[$\bar{1}$10]-direction and along the W[001]-direction, respectively. The radii of curvature were measured on two differently cut crystals along [$\bar{1}$10] and along [001] during film growth, as shown in figure 10(*a*). Quite surprisingly, the growth of Fe induces compressive stress in the submonolayer range along [001], but tensile stress along [$\bar{1}$10]. An anticlastic curvature of the W crystal results, figure 10(*b*). This result indicates that strain arguments, that predict tremendous tensile stress, are of diminished importance in the submonolayer range. Here, surface-stress effects govern the stress behaviour [179, 224, 225]. Only for coverages above 0.5 ML does a tensile stress set in along both directions. The slope of the curves in figure 10(*c*) indicate an anisotropic tensile stress of 65 GPa along [$\bar{1}$10] and of 44 GPA along [001]. For simplicity, we assume a Fe-monolayer thickness of 2 Å, which is the average of the experimental data of the Fe–W distance (1.94 Å [222], 2.07 Å [223]). These stress values are more than 60% larger than the continuum elasticity predicts. However, one has to remember that the stress in the first monolayer is measured and it is certainly a rough estimate to employ bulk elasticity to monolayers and neglecting the important contribution of surface-stress effects. The kink in the curve at 1.2 ML is the direct experimental evidence for the stress relief due to the beginning formation of misfit distortions in the film. Curvature measurements indicate the structural change in the film with high sensitivity. The stress measurements of figure 10 suggest, that the second and third Fe layers grow practically stress free, as indicated by the almost horizontal slope of the curve in that coverage region. A constant isotropic stress of order 13 GPa is

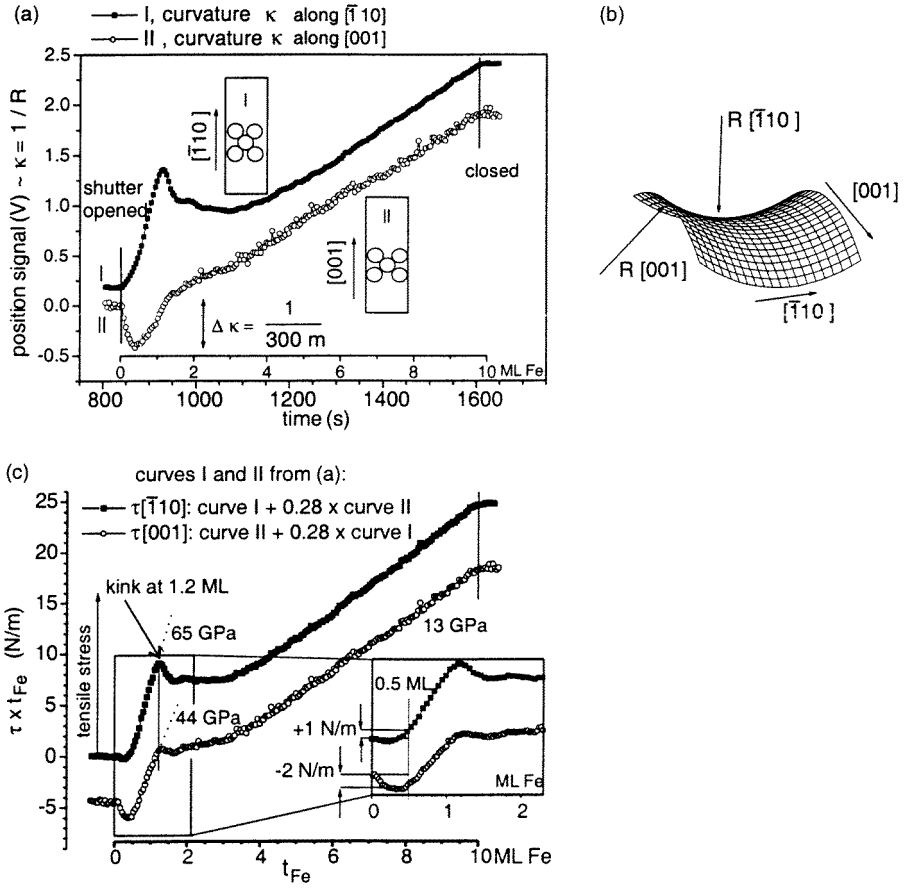

Figure 10. Stress measurement during the growth of Fe on W(110) at 300 K. (*a*) The substrate curvature is monitored during film growth on two differently oriented crystals. Note the opposite sign of the curvatures in the submonolayer range, that lead to an anticlastic deformation of the substrate shown in (*b*). (*c*) Both curvature data of (*a*) have to be combined with the Poisson ratio of W ($\nu = 0.28$) to obtain the stress components. The film stress is given by the slope of the curves, values are quoted for the anisotropic monolayer region, and the isotropic stress from 4 ML to 10 ML. The kink in the curve at 1.2 ML indicates the formation of misfit distortions. The inset shows the opposite sign of the Fe-induced stress in the submonolayer range. After [179].

measured for the fourth up to the tenth monolayer.

LEED [221] and STM [226–228] reveal the atomic nature of the misfit distortions that are formed in the Fe film at 1.2 ML as additional lines of Fe atoms that are first inserted along the [001] direction in the second layer. The first Fe layer is expected to remain pseudomorphically strained. In the third Fe layer, a periodic two-dimensional distortion line network evolves that is identified in the LEED and STM image of 3 ML Fe on W(110) presented in figure 11 [224].

The stress measurements reveal that the introduction of misfit distortions relaxes the film stress almost completely in the second Fe layer. The STM analysis shows that distortion lines are spaced on a nm-scale in the Fe film. Consequently, the resulting spatial variation of the film strain can be expected to be very complicated. For example, the strain of Fe islands of the second layer might already be relaxed, whereas the underlying first layer remains strained by more than 10%. Thus, stress variations of order 40 GPa seem possible on a nm-scale once

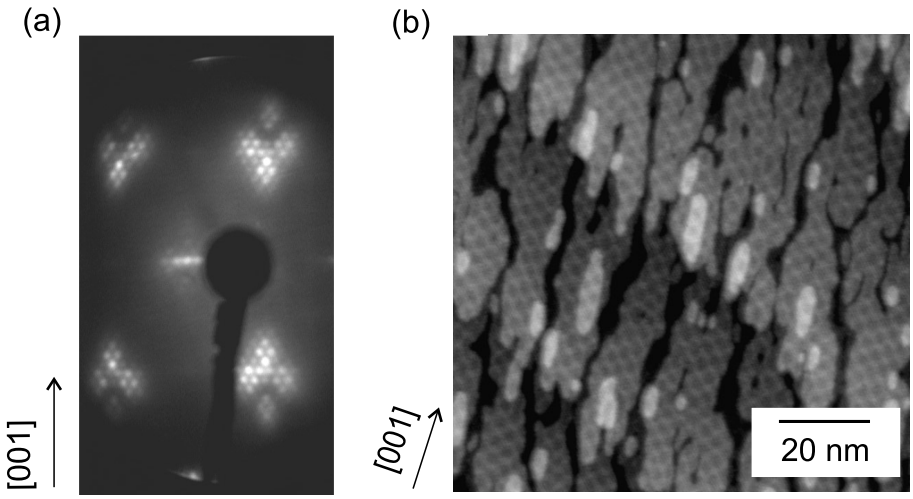

Figure 11. Distortion network of 3 ML Fe on W(110). Growth temperature 300 K. The LEED image (*a*) shows additional diffraction spots that are arranged in a diamond area around the bcc(110)-diffraction spots. (*b*) The STM image shows elongated islands of the third layer (grey), and patches of the fourth layer (lighter grey) with an regular arrangement of distortion lines in lighter grey. After [224].

the critical thickness for the introduction of misfit distortions of order 1.2 ML is reached. One has to expect that this nanoscale strain variation might influence the magnetic properties of so-called sesquilayers (1.5) of Fe considerably via the magneto–elastic coupling.

The magnetic anisotropy of the sesquilayer films can be expected to differ substantially from the pseudomorphically strained first layer, or from the stress-relaxed thicker Fe films. To estimate the influence of varying strains on the anisotropy it is necessary to know both film strain *and* the magneto–elastic coupling coefficients B_1 and B_2 *in the monolayer range*. The magneto–elastic energy density of a cubic film can be described by $f_{\rm me} = B_1(\epsilon_1\alpha_1^2 + \epsilon_2\alpha_2^2 + \epsilon_3\alpha_3^2) + B_2(\epsilon_4\alpha_2\alpha_3 + \epsilon_5\alpha_1\alpha_3 + \epsilon_6\alpha_1\alpha_2)$, see (3.1). The cubic strains ϵ_i have to be expressed in terms of the in-plane film strains $\epsilon_{1,\rm F} = \epsilon_{2,\rm F}$ by performing the same tensor transformation as presented in section 2. The directions cosines α_i of the magnetization direction with respect to the cubic axes have to be calculated for the different magnetization states for which the magneto–elastic anisotropy has to be calculated. Inserting the expression for the vertical film strain $\epsilon_{3,\rm F}$ as a function of the in-plane strains, see section 2, and denoting the in-plane film strains ϵ_0, the following magneto–elastic contributions to the in-plane and out-of-plane anisotropy of cubic (110) films result:

$$\begin{aligned} k_{\rm me}^{\text{in-plane}} &= f_{\rm me}(M_{001}) - f_{\rm me}(M_{\bar{1}10}) = \frac{(c_{11}+2c_{12})}{c_{11}+c_{12}+2c_{44}}(B_1 - B_2)\epsilon_0 \\ k_{\rm me}^{\text{out-of-plane}} &= f_{\rm me}(M_{001}) - f_{\rm me}(M_{110}) = \frac{(c_{11}+2c_{12})}{c_{11}+c_{12}+2c_{44}}(B_1 + B_2)\epsilon_0 \\ k_{\rm me}^{\text{out-of-plane}} &= f_{\rm me}(M_{\bar{1}10}) - f_{\rm me}(M_{110}) = 2\frac{(c_{11}+2c_{12})}{c_{11}+c_{12}+2c_{44}}B_2\epsilon_0. \end{aligned} \tag{6.1}$$

Equation (6.1) describes the difference of the anisotropy energy for different magnetization directions that are indicated by M_{ijk} as a function of the in-plane film strain ϵ_0, and the

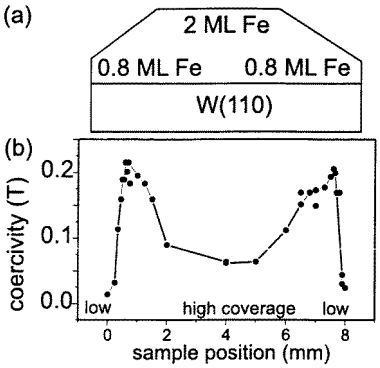

Figure 12. Coercivity of Fe/W(110), measured at 140 K on a film with a mesa-shaped thickness variation. (*a*) Sketch of the film thickness as determined by Auger-electron spectroscopy versus the sample position. (*b*) Note the pronounced maxima of the coercivity at the two sample positions where the thickness crosses the sesquilayer range. After [151].

magneto–elastic coupling coefficients B_i. The elastic constants of the film c_{ij} enter, as the perpendicular film strain has been expressed in terms of the in-plane strain. The fraction of the elastic constants is of order unity, the exact value for Fe is $(c_{11} + 2c_{12})/(c_{11} + c_{12} + 2c_{44}) = 0.838$. A positive value of k is caused by a smaller energy contribution for the second magnetization direction which indicates a magneto–elastic anisotropy contribution that favours the magnetization direction that is indicated in the second term.

One might wonder whether the pseudomorphic strain of ≈10% in the monolayer of Fe favours a perpendicular film magnetization. To check the magneto–elastic contribution to the anisotropy, we consult the expression given in (6.1), as the easy axis of magnetization in ultrathin Fe films on W(110) is known to be $[\bar{1}10]$. Inserting the values for bulk Fe, $B_2 = 7.62$ MJ m^{-3} gives the tremendous anisotropy energy density of $f_{\rm me} = 1.28$ MJ m^{-3}. This strain-induced anisotropy is a factor of 25 larger than the magneto–crystalline anisotropy of Fe ($K_1 = 0.05$ MJ m^{-3} [63]) and justifies the consideration of strain-induced changes of the easy axis of magnetization. The positive value of k shows that a tensile film strain will indeed favour a perpendicular magnetization of the film, *provided that B_2 does not change its sign in the monolayer range*. To derive a crude estimate as to whether the magneto–elastic anisotropy will lead to a perpendicular anisotropy, one has to compare the sum of stray-field energy density $\frac{1}{2}\mu_0 M_{\rm S}^2 = 1.93$ MJ m^{-3} and surface anisotropy $K_{\rm S}/t_{1\ {\rm ML}} = 5$ MJ m^{-3} [229] with the strain-induced anisotropy of $f_{\rm me} = 1.28$ MJ m^{-3}. The bulk value of B_2 is not sufficient to induce a perpendicular film magnetization, its value has to be more than five times larger to compensate the stray field and the surface anisotropy energy contributions [218]. However, one has to be aware of the limitation of such a crude phenomenological model in the monolayer range.

Our results on the modified magneto–elastic coupling in Fe(100) monolayers on W(100), that are presented in the next section, indicate that the magneto–elastic coupling coefficients cannot be assumed to remain at their bulk values for monolayer films. Rather, the sign and magnitude of B_1 were found to change [10,187]. In conclusion, the lack of experimental data on B_1 and B_2 of strained Fe monolayers inhibits a quantitative discussion of the magneto–elastic contribution to the peculiar magnetic behaviour of sesquilayer Fe films. A rough estimate of the contribution of the inhomogeneous stress field to the coercivity of the sesquilayer Fe films is derived below.

However, the film morphology is another important factor that determines the magnetic anisotropy [230–232]. The film morphology in the sesquilayer region is characterized by a local varying film thickness between one and two layers. This spatial variation of the film thickness is found to induce the high coercivity of 1.5 ML Fe that is discussed next.

Figure 12 shows a plot of the variation of the coercivity of an Fe film on W(110) in the

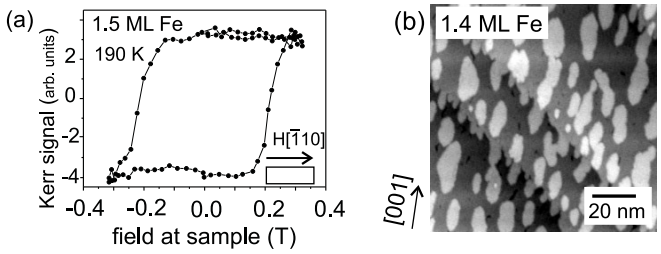

Figure 13. (*a*) Kerr hysteresis loop of 1.5 ML measured at 190 K. (*b*) STM image of 1.4 ML Fe on W(110). Patches of the second Fe layer (lighter grey) are seen on the first Fe layer (darker grey). The lines running from the upper left to the lower right are monoatomic steps of the W-substrate. After [224].

thickness range 0.8–2 ML. The sample was moved in front of the evaporator to obtain this mesa-shaped film thickness variation over a length of 8 mm, as shown in figure 12(*a*). The coercivity of the film was measured as a function of position by scanning the laser beam of the Kerr experiment over the length and taking subsequent Kerr loops at 140 K. Pronounced maxima of the coercivity were found where the film thickness crossed the sesquilayer range. Figure 13(*a*) shows a magnetization curve of a single 1.5 ML Fe film. Note that the coercivity is larger than 0.2 T at 190 K. At 140 K, we could not overcome the even larger coercivity at the lower temperature. The STM image of figure 13(*b*) shows the morphology of an Fe film at a coverage of 1.4 ML. Second-layer Fe islands (grey) are shown on the first Fe monolayer (darker grey) that covers the W-crystal homogeneously. The lateral dimensions of the Fe patches are anisotropic with a larger extension along [001] of the order of 20 nm, whereas in the perpendicular direction, a width of the patches of the order of 10 nm is observed. The elongated shape of pseudomorphically strained Fe patches might be partially ascribed to the anisotropic film stress that is calculated and measured to be ≈40% smaller along [001]. Therefore, a smaller strain energy in the patch results for an extension along [001] versus an extension along [$\bar{1}$10]. Additional contributions to an anisotropic growth might arise from anisotropic Fe diffusion on (110) surfaces, that was investigated at high temperatures by Reuter *et al* [233, 234].

To explain the high coercivity at the sesquilayer coverage of 1.5 ML, one has to realize that the magnetization process proceeds via the propagation of 180° Néel walls in the Fe film. We arrive at this conclusion as the lower coercivity of the 1 ML and 2 ML films, see figure 12(*b*), indicates the presence of nucleation centres of domains with reversed magnetization. The spatial variation of the layer thickness from one to two layers over distances that are larger than the domain wall width leads to a strong pinning of the domain walls in the patches of the second layer. There, the domain wall energy γ is increased due to the larger film thickness t: $\gamma = 4\sqrt{2K_S At}$ [151]. The in-plane surface anisotropy is given by $K_S = 0.6$ mJ m^{-2} [229], the exchange interaction is $A = 10^{-11}$ J m^{-2}, and t denotes the film thickness. A maximum coercivity of $H_C \leqslant 2K_S/(\pi\mu_0 M_S t) = 0.59$ T, (M_S : saturation magnetization), can be estimated [151]. This increase of the coercivity is due to the enhanced exchange interaction in the two-layer patches. A similar pinning mechanism was proposed to account for the high coercivity in ultrathin Co films, sandwiched between Au [231].

A rough estimate of the influence of the inhomogeneous stress field of the sesquilayer film concludes this section. The stress measurements of figure 10(*c*) indicate that the introduction of misfit distortion relaxes the film stress almost completely in the second layer. Thus, the film strain can be estimated to vary by 10%. If we ascribe tentatively the large in-plane anisotropy

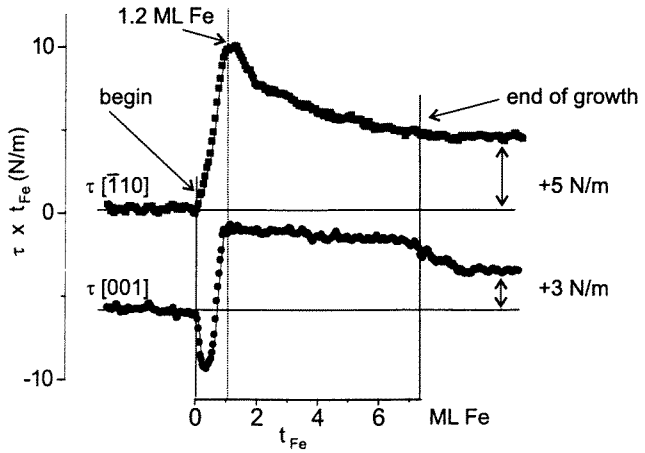

Figure 14. Stress during Fe growth on W(110) at 1000 K. Note the sharp kink in the curve after the completion of the first monolayer. The deposition of more Fe does not increase the film stress anymore. After termination of growth, a partial stress relaxation is observed for $\tau[001]$. The final stress value corresponds to the stress induced by the first ML. After [215].

of the pseudomorphic Fe layer to the the distortion of the (110)-surface with respect to the cubic (100)-surface which has a significant lower in-plane anisotropy, one concludes that the nominal strain of $\sqrt{2} - 1 = 41\%$ of the atoms in a (110) film induces $K_S = 0.6$ mJ m^{-2}. Assuming further a linear relation between the in-plane anisotropy and the lattice deformation [235], the strain variation of 10% induces a coercivity of $0.59\ \mathrm{T}/4.1 = 0.14$ T. Thus, the stress contribution to the coercivity is smaller than the crystalline contribution discussed above, but not necessarily negligible [151].

6.2. Stranski–Krastanov growth at higher temperatures and the in-plane reorientation of the easy axis of magnetization

The growth of Fe on W(110) at room temperature leads to the formation of misfit distortions in the second layer of Fe, as indicated by the kink in the stress curve presented in figure 10. Note, that the horizontal section of the stress curves reveals a practically stress-free growth of the second, third and fourth layer of Fe at room temperature. For higher coverages, an isotropic tensile stress of 13 GPa is measured, see figure 10(*c*). However, if Fe is deposited at a higher substrate temperature of 1000 K, only the pseudomorphically strained first monolayer contributes to the measured film stress. The stress curves obtained from the analysis of the curvature measurements performed at a substrate temperature of 1000 K are presented in figure 14.

In contrast to room-temperature growth, the final stress value corresponds to the stress induced by the first monolayer deposited at 1000 K. The reason for this effective reduction of the film stress is given by the structural analysis of the film structure in figure 15. In sharp contrast to the almost layer-by-layer growth of Fe on W(110) at room temperature, the growth at higher temperature leads to the so-called Stranski–Krastanov growth: Fe islands are formed on the pseudomorphically strained monolayer, that covers the W substrate homogeneously [236]. A double-LEED pattern results, see figure 15(*a*), with the diffraction pattern of a bcc(110) W lattice constant, inner diffraction spots, and with a second, outer set of diffraction spots that indicate a relaxed lattice constant of Fe. The STM image of figure 15(*b*) shows elongated

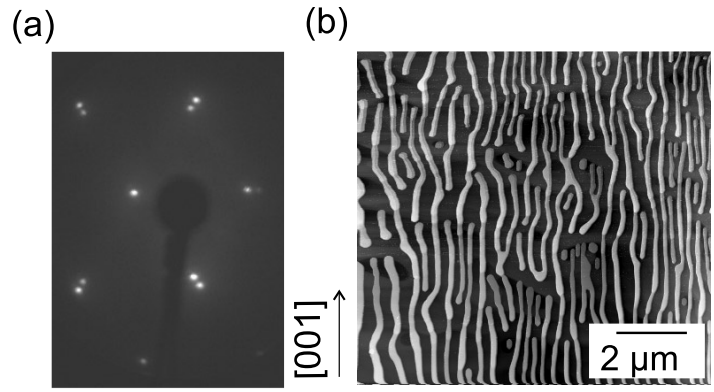

Figure 15. LEED (*a*) and STM image (*b*) of annealed Fe films, deposited at room temperature on W(110). (*a*) Two sets of bcc(110) diffraction spots indicate two lattice constants of the island structure shown in (*b*). Elongated and strain-relaxed Fe islands (lighter grey) are shown on the first pseudomorphically strained Fe monolayer (dark grey), that covers the W substrate. After [186].

Fe islands, that were observed either after growth at 1000 K, or after annealing a room-temperature grown Fe film to 700–1000 K. The Stranski–Krastanov growth leads to Fe islands of μm length and $\approx$100 nm width, that are extended along [001]. The double-diffraction image of figure 15(*a*) is ascribed to the superposition of the diffraction images from the strain-relaxed Fe from the top of the islands and from the pseudomorphically strained Fe from the Fe monolayer, that covers the W substrate between the islands. Scanning Auger microscopy proved that one Fe monolayer is thermally stable and remains on the W surface between the islands [234] up to the desorption temperature of 1400 K [237].

The driving force for the structural transition from layer-by-layer growth to island growth can be ascribed to the reduction of the strain energy in the Fe film, as corroborated by the practically stress-free growth at higher temperature, in contrast to the significant stress measured in Fe films that were deposited at room temperature. This stress-driven structural transition leads to a change of the easy axis of magnetization of the Fe islands. MOKE measurements on 1.7 nm thin Fe film were performed after deposition at room temperature, upper panel of figure 16, and after annealing for several minutes to 700 K, lower panel of figure 16. MOKE measurements were performed in the transversal, longitudinal, and polar configuration to investigate the film magnetization along the in-plane [$\bar{1}$10], [001] and the out-of-plane [110] direction, respectively.

The hysteresis curves of figure 16 show an in-plane reorientation of the easy axis of magnetization due to the annealing of the film [186,238]. We ascribe this in-plane reorientation of the easy axis of magnetization to the diminished importance of the so-called surface anisotropy in the thick Fe islands. Annealing the film leads to an increase of the Fe thickness in the Fe islands as compared with the nominally deposited amount of Fe. Therefore, the contribution of the surface anisotropy that favours the in-plane [110] easy axis [216, 239], loses its weight with the increased layer thickness, and the [100] easy magnetization direction is observed, as in bulk Fe. Note, that in addition to the fading influence of the surface anisotropy, the shape anisotropy of the elongated Fe islands favours an easy axis of magnetization along [001] [215, 240] due to the large length-to-width ratios of the islands. Finally, the stress-free growth of the Fe islands at higher temperatures indicates in conjunction with our LEED

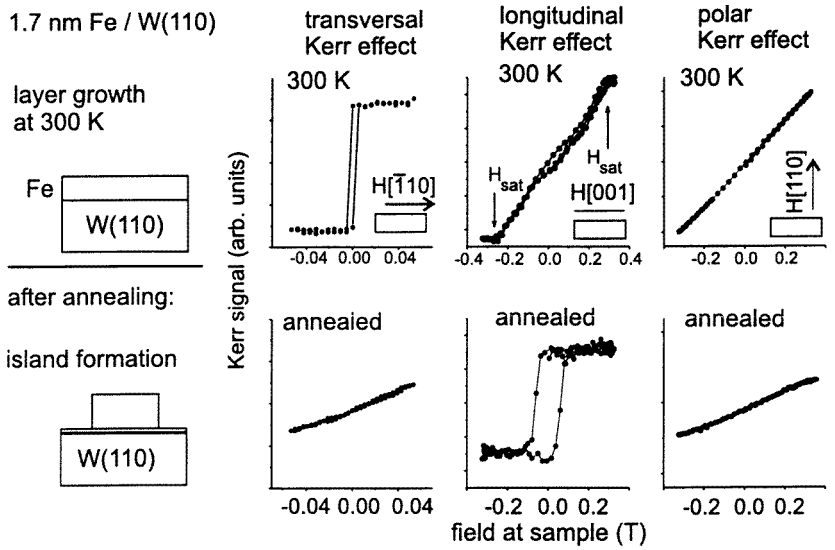

Figure 16. MOKE measurements on 1.7 nm Fe on W(110), after growth at room temperature, upper panel, and after annealing the same film to 700 K for several minutes, lower panel. The as-grown film shows an easy axis of magnetization along [$\bar{1}$10], whereas after annealing the the easy axis reorients in-plane towards [001], as indicated by the rectangular magnetization curve. After [186].

data that the Fe islands are under negligible in-plane strain. Thus, the film strain ϵ_0 as a possible magneto–elastic driving force of the in-plane anisotropy, as indicated by (6.1), is not operative in the islands and—neglecting possible surface and interface anisotropies—the in-plane anisotropy is governed by the bulk crystalline anisotropy, favouring the [100] easy magnetization direction.

In conclusion, stress-driven structural transitions like the formation of misfit distortions or the change of the growth mode induce characteristic changes of the magnetic behaviour of ultrathin Fe films on W(110). In the following section the *direct* impact of film strain on the magnetic properties is discussed for the strain-dependent magneto–elastic coupling in epitaxial Fe films.

7. Strain-induced changes of the magneto–elastic coupling

The magneto–elastic coupling coefficients are known as material constants of *bulk* materials. In ultrathin films however, or within Å near the surface of a bulk sample, the magneto–elastic coupling has been found to differ substantially in magnitude and even in sign from the respective bulk value. A short compilation of the experimental data and phenomenological models that support a stress and film thickness dependent correction of the magneto–elastic coupling coefficients was presented in section 3. In this section, experimental data on the modified magneto–elastic coupling in epitaxial Fe(100) films are presented that underline the importance of film strain for the peculiar magneto–elastic coupling measured in nm thin Fe.

The application of tensile stresses in the GPa range was found to lower the saturation magnetization of amorphous Co-rich alloys [103,104]. The magnetostriction of Co multilayers was found to decrease to more negative values with decreasing film thickness [193], and the magnitude of the magneto–elastic coupling was found to be more positive by factors of

≈3 near the surface region of amorphous alloys [5]. Thus, Néel type models of surface magnetostriction were developed [6], that lead to a reciprocal thickness dependence of the magneto–elastic coupling. Both effects, Néel-type surface corrections *and* strain corrections to the magneto–elastic coupling coefficients were introduced [100]. Recent measurements of the magnetostrictive bending of epitaxial Fe films on MgO(100) by Koch *et al* clearly suggest that the film stress is of utmost importance to account for the deviation of the magneto–elastic coupling coefficient from its bulk value [9]. Further evidence for the important role of film strain for the strain-dependent corrections of these coefficients is presented below.

The *in situ* combination of the bending beam technique with magnetization measurements, see section 5, enables the direct correlation between film stress and magnetostrictive bending. The film stress is measured during growth from the curvature of the substrate, and assuming linear elasticity theory to apply, the stress data can be converted into strain data with the help of the equations given in section 2. Note, that the curvature signal that is measured during film growth as a function of time, is proportional to $\tau \times t_F$. Thus, the slope of the position signal indicates the film stress in the growing layer. A plot of film stress versus film thickness can be obtained from the curvature measurement. This analysis requires, that the formation of misfit distortions does not alter the stress state of the underlying layers. This assumption seems to be valid for the growth of Fe on W at room temperature, where no stress relaxation due to a restructuring of the whole film is observed. At growth temperatures above 500 K however, a partial stress relaxation is observed *after termination of growth*, indicating thermally activated stress relaxation processes in the whole film [186]. Different structural components have been identified in the Mössbauer analysis of Fe(110) films on W(110) by different magnetic hyperfine fields [241]. The authors claim that their study of the magnetic hyperfine fields in Fe layers indicate the structural stability of the first monolayer even in the presence of misfit distortions in thicker films. This result supports our simplified approach, that at room-temperature structural changes do not change the stress state of underlying layers significantly, and the slope of the stress curve at a given thickness can be attributed to the stress in that layer. At the end of this section we discuss an alternative to this layer-resolved stress analysis that simply takes the final change of the film stress at the end of the growth process into account to derive an average stress of the film.

The stress measurements during growth of Fe on W(100) presented in figure 17 indicate that in contrast to the growth on W(110), the first *three* monolayers grow pseudomorphically strained, until the formation misfit distortions induce a kink in the curve. This upper limit of the pseudomorphic growth of ≈3 ML is in agreement with previous work on the magnetic and structural properties of Fe monolayers on W(100) [242–244]. First STM investigations on the growth of Fe on W(100) show an island growth of Fe [64], in contrast to the layer growth of Fe observed on W(110) [217, 226]. Thus, the unexpectedly high layer thickness of ≈3 ML that can sustain the tremendous epitaxial misfit strain can be ascribed to the abundance of Fe islands, that might allow for some strain relaxation at the islands edges.

The initial compressive stress in the first monolayer, as indicated by the negative slope of the stress curve in figure 17(*a*) is ascribed to a surface-stress effect [179]. The positive slope in the subsequent section corresponds to a tensile film stress of 10 GPA. This is only half of the film stress that is expected from the misfit strain of $\epsilon = 10.4\%$, which is calculated to induce a film stress of $\tau = Y_{Fe}/(1-\nu_{Fe})\epsilon = 21$ GPa, see table 1. The discrepancy between the measured stress and the calculated stress might be tentatively assigned to the island growth, which leads to a smaller effective strain in the film due to the possibility of strain relaxation. Thus, we apply continuum elasticity to calculate the average effective strain in each layer from the slope of figure 17(*a*), the result is plotted in figure 17(*b*). The grey shaded area indicates the thickness range where misfit distortions are formed, separating two constant-strain regimes, region I:

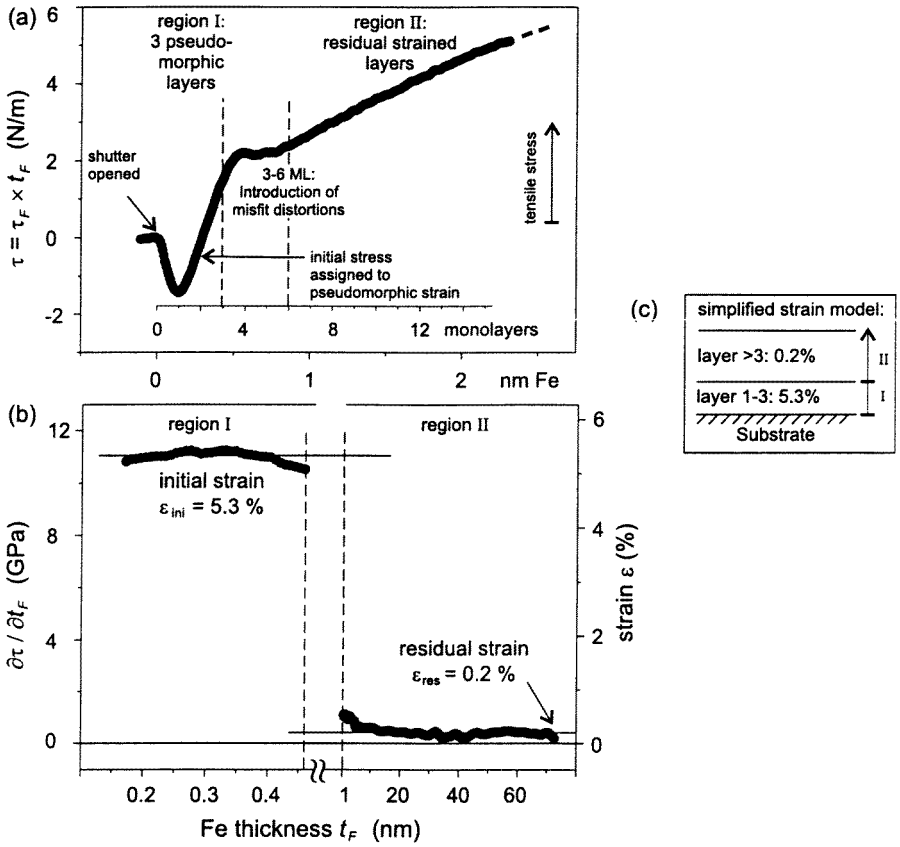

Figure 17. Film stress τ and film strain ϵ as a function of Fe film thickness. (*a*) Film stress during the growth of Fe on W(100) at room temperature. The kink in the curve at 4 ML indicates the end of pseudomorphic growth and the formation of misfit distortions. (*b*) The positive slope of (*a*) indicates an initial strain of 5.3%, after the formation of misfit distortions, an almost constant residual strain of 0.2% is calculated. (*c*) Simplified strain model: the first three layers are strained by 5.3%, the higher layers are described by a constant strain of 0.2%. After [194].

pseudomorphic growth with an *effective* strain of 5.3%, and region II: residual strain of 0.2%. The striking point of this strain analysis is that the strain in the Fe layer drops in a very narrow thickness range of only 0.5 nm to the almost constant residual strain of 0.2%. The result of two almost constant strain values in the film is at variance with the usually assumed continuous strain relaxation with increasing film thickness [166, 231, 245], that we used earlier [187]. A similar, almost step-like decrease of the film strain within a narrow thickness range of only $\approx$2 ML was recently found in LEED studies on the growth of epitaxial Ni films [55]. This *direct* strain measurement by LEED corroborates our strain analysis that is based on a stress measurement.

The magneto–elastic coupling coefficient B_1 was measured by analysing the magnetostrictive bending of the film–substrate composite while the film magnetization was switched along the sample length and the sample width in Fe [100] directions [186]. Equation (5.5) was used to derive the values for the magneto–elastic coupling coefficient presented in figure 18 as a function of film thickness.

In sharp contrast to the constant value of $B_1 = -3.44$ MJ m^{-3} of bulk Fe, a strong

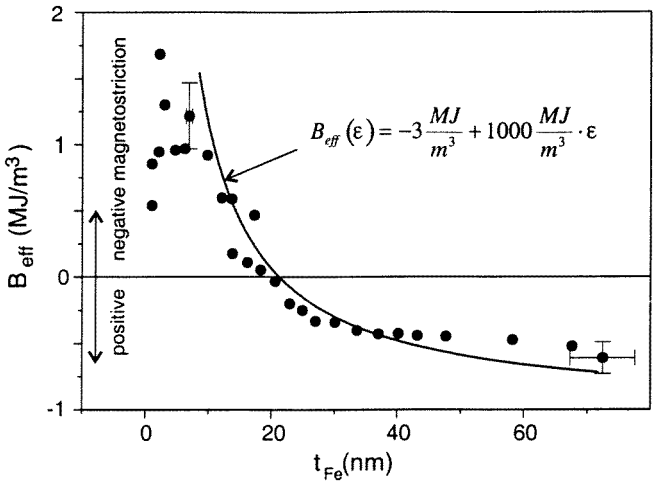

Figure 18. Effective magneto–elastic coupling coefficient $B_{\rm eff}$ as a function of the Fe film thickness. The magneto–elastic coupling has a zero-crossing at ≈20 nm, being negative at higher film thickness, and being positive at smaller thickness. Bulk Fe: $B_1 = -3.44$ MJ m^{-3}. The solid curve is given by a strain-dependent correction of $B_{\rm eff} = B_1 + D\epsilon$ with $D = 1000$ MJ m^{-3}. The thickness information was replaced by the thickness dependence of the strain shown in figure 17(*b*). After [215].

thickness dependence of the magneto–elastic coupling is shown in figure 18. Fe films thicker than 20 nm induce compressive magnetostrictive stress, indicated by negative values of $B_{\rm eff}$, films thinner than 20 nm induce tensile magnetostrictive stress, in contrast to the bulk behaviour. At a thickness of 20 nm, *no* magnetostrictive stress is measured, $B_{\rm eff} = 0$. We ascribe this apparent thickness dependence of $B_{\rm eff}$ to a strain-dependent correction of B_1, $B_{\rm eff} = B_1 + D\epsilon$ [9,10,100,102]. The film strain is known for each data point in figure 18 from the analysis of figure 17 with $\epsilon = 5.3\%$ for films thinner than 1 nm, and $\epsilon = 0.2\%$ for thicker films. It is assumed that each layer n contributes to the effective magneto–elastic coupling with the respective strain correction, $B_{\rm eff}(N) = \frac{1}{N}\sum_{i=1}^{n}(B_1 + D\epsilon_n)$, where the total number of layers is given by N. Using a value for $B_1 = -3$ MJ m^{-3} that is slightly smaller than the bulk value of B_1 and $D = 1000$ MJ m^{-3} from [9], the solid curve in figure 18 results, which describes the experimental data for $t_{\rm Fe} > 10$ nm with fair agreement. This strain-dependent correction of B_1 suggests a continuing increase of $B_{\rm eff}$ for the higher strained thinner films, which was not found in the experiment. However, $B_{\rm eff}$ remains positive for decreasing film thickness down to 3 ML, which marks the limit of resolution of our magnetostrictive bending experiment [215].

Unfortunately, no rigorous justification for the derivation of the thickness-resolved strain from stress measurements can be presented. The reason is that the thickness-resolved information on film strain is not *directly* accessible in experiments. Therefore, we present in the following an alternative analysis of the film stress measurement [10]. Instead of exploiting the slope of the curvature versus thickness curves one could consider only the change of the substrate curvature measured between the beginning and the end of the film growth. This analysis can be performed on one stress curve at different thicknesses because no stress relaxation is observed at room temperature, as checked by interrupted growth experiments. Performing the same analysis on separately prepared films of different thickness gives the same stress versus thickness curve. The result is presented in figure 19(*a*). This analysis gives

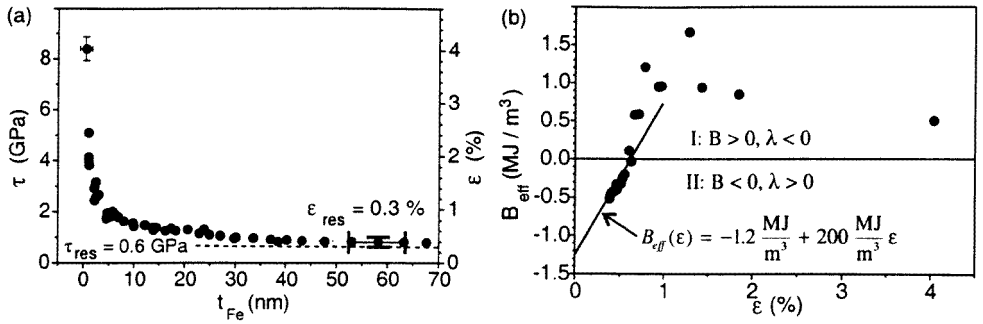

Figure 19. Simplified stress analysis. (*a*) Average film stress, left axis, and film strain, right axis, of Fe(100) on W(100), grown at 300 K. (*b*) Effective magneto–elastic coupling, B_{eff} data from figure 18, as a function of film strain. A linear strain correction of B_{eff} is deduced from the slope and the intercept of the linear curve for $\epsilon < 0.6\%$. After [10].

a more gradual decrease of the film strain as compared with the step-like behaviour shown in figure 17(*b*). The gradual decrease of the film strain allows us to plot the magneto–elastic coupling coefficient B_{eff} versus the film strain ϵ to check whether a linear strain correction of B_1 is found. To this end, the thickness scale of figure 18 is converted to a strain scale using the data of figure 19(*a*). Figure 19(*b*) shows the strain dependence of B_{eff}. A linear strain dependence is found only for strains smaller than 0.6%, as indicated by the linear fit in this strain regime. The slope of the solid curve gives $D = 200 \pm 30$ MJ m^{-3} and the intercept of the vertical axis gives $B_1 = -1.2 \pm 0.2$ MJ m^{-3} [10]. This simple linear correction fails to describe the experimental data for strains larger than 0.6%, which translates to a film thickness below 15 nm.

The deviation of B_{eff} from the linear strain correction models presented in figures 18 and 19(*b*) indicates the severe limitations of such phenomenological models in the monolayer range. It remains to be investigated to what extent possible interface and surface effects are responsible for the peculiar magneto–elastic behaviour of the first layers.

In any case, however, the magneto–elastic coupling in epitaxial Fe(100) films is found to deviate both in magnitude *and* sign from the respective bulk value. It is important to note, that the large magnitude of D induces significant corrections of B_1 *even for small strains in the sub-% range*. Therefore, it should not be expected that bulk magneto–elastic constants apply to epitaxially strained films, even when the strain is relatively small.

8. Conclusion and outlook

The analysis of the stress-induced bending of film–substrate composites has been compiled for the determination of both epitaxially induced misfit stress *and* magneto–elastic coupling in monolayer thin films. Stress measurements with sub-monolayer sensitivity have proven the diminished importance of strain arguments for the measured film stress in the sub-monolayer range. It is proposed that the classical stress–strain relations have to be modified by the inclusion of surface-stress effects to explain measured film stress that is of opposite sign as expected from lattice mismatch arguments. These new experimental results remain a challenge for *ab initio* calculations on adsorbate-induced stresses, and the relevant physical processes that govern stress at sub-monolayer coverages are still not well established. With increasing coverage, the curvature analysis has been demonstrated to be a simple tool to measure film stress and to detect structural transitions like the formation of misfit distortions or the change

of the growth mode from layer-by-layer growth to island growth with high sensitivity. Film stress has been identified as an important driving force for structural transitions. Stress–strain relations have been derived for various epitaxial orientation that allow a calculation of film strain from a measurement of film stress.

Measurements of the magnetostrictive bending of ultrathin epitaxial Fe films indicate that magnitude and sign of the magneto–elastic coupling coefficients deviate sharply from the respective bulk values. The combined measurement of film stress *and* magnetostrictive bending in one experiment has been shown to provide important insight into the dominant role of epitaxial strain for the modified magneto–elastic coupling in ultrathin films. The implications of modified magneto–elastic behaviour in ultrathin films are profound as one has to accept from the experimental results that *bulk magneto–elastic coupling coefficients do not apply to ultrathin films in general*. One important consequence of this result is that the strain-induced anisotropy which is phenomenologically treated in view of the magneto–elastic coupling, cannot be predicted from bulk behaviour. Experimental data on the relevant magneto–elastic coupling coefficients are clearly called for. It remains a challenge for future experimental and theoretical work to investigate the electronic origin of the strain and possibly thickness dependence of the relevant magneto–elastic coupling coefficients.

It remains to be experimentally confirmed whether the pronounced strain-dependence of the magneto–elastic coupling coefficient B_1, that is found to change magnitude and sign of the effective magneto–elastic coupling in epitaxial Fe films, is also measured for other epitaxial films. The stunning sequence of reorientations of the easy axis of magnetization in epitaxial Ni films on Cu(100) with increasing film thickness from in-plane to perpendicular at $t = 7$ ML to in-plane again at $t = 60$ ML [51] represents an ideal test for the discussion of magneto–elastic effects. A *direct* measurement of both, film stress *and* magnetostrictive stress could clarify the contribution of surface magneto–elastic corrections [53] versus strain-induced corrections of the the magneto–elastic coupling in Ni monolayers.

Acknowledgments

I am pleased to acknowledge Jürgen Kirschner for his continuous support and his vivid interest in our work. Most of the experiments were done in close cooperation with Axel Enders. I appreciate his experimental efforts that were the basis of many results that were presented.

Appendix

The inverse matrices of (2.3) and (2.4) give the contracted compliance matrices for the cubic and hexagonal class, respectively. For the cubic class:

$$s_{ij}^{\text{cubic}} = \begin{pmatrix} s_{11} & s_{12} & s_{12} & 0 & 0 & 0 \\ s_{12} & s_{11} & s_{12} & 0 & 0 & 0 \\ s_{12} & s_{12} & s_{11} & 0 & 0 & 0 \\ 0 & 0 & 0 & s_{44} & 0 & 0 \\ 0 & 0 & 0 & 0 & s_{44} & 0 \\ 0 & 0 & 0 & 0 & 0 & s_{44} \end{pmatrix} \tag{A.1}$$

$$\begin{aligned} s_{11} &= \frac{(c_{11} + c_{12})}{(c_{11} + 2c_{12})(c_{11} - c_{12})} \\ s_{12} &= \frac{-c_{12}}{(c_{11} + 2c_{12})(c_{11} - c_{12})} \\ s_{44} &= 1/c_{44}, \end{aligned} \tag{A.2}$$

and for the hexagonal class:

$$s_{ij}^{\text{hexagonal}} = \begin{pmatrix} s_{11} & s_{12} & s_{13} & 0 & 0 & 0 \\ s_{12} & s_{11} & s_{13} & 0 & 0 & 0 \\ s_{13} & s_{13} & s_{33} & 0 & 0 & 0 \\ 0 & 0 & 0 & s_{44} & 0 & 0 \\ 0 & 0 & 0 & 0 & s_{44} & 0 \\ 0 & 0 & 0 & 0 & 0 & 2(s_{11}-s_{12}) \end{pmatrix} \tag{A.3}$$

$$\begin{aligned} s_{11} &= \frac{(c_{11}c_{33}-c_{13}^2)}{(c_{11}c_{33}+c_{12}c_{33}-2c_{13}^2)(c_{11}-c_{12})} \\ s_{12} &= \frac{-(c_{12}c_{33}-c_{13}^2)}{(c_{11}c_{33}+c_{12}c_{33}-2c_{13}^2)(c_{11}-c_{12})} \\ s_{13} &= \frac{-c_{13}}{(c_{11}c_{33}+c_{12}c_{33}-2c_{13}^2)} \\ s_{33} &= \frac{(c_{11}+c_{12})}{(c_{11}c_{33}+c_{12}c_{33}-2c_{13}^2)} \\ s_{44} &= 1/c_{44}. \end{aligned} \tag{A.4}$$

Note, that in contrast to the contracted matrix notation of the c_{ij} for the s_{ij} factors of two and four are introduced [58]:

$$\begin{aligned} s_{ijkl} &= s_{mn} \qquad m=1,2,3, \qquad \text{and} \qquad n=1,2,3, \\ 2s_{ijkl} &= s_{mn} \qquad m=4,5,6, \qquad \text{or} \qquad n=4,5,6, \\ 4s_{ijkl} &= s_{mn} \qquad m=4,5,6, \qquad \text{and} \qquad m=4,5,6. \end{aligned} \tag{A.5}$$

References

[1] Bozorth R M 1993 *Ferromagnetism* (Piscataway, NJ: IEEE)
[2] Lee E W 1955 *Rep. Prog. Phys.* **18** 184-229
[3] Kneller E 1962 *Ferromagnetismus* (Berlin: Springer)
[4] Jiles D C and Atherton D L 1984 *J. Phys. D: Appl. Phys.* **17** 1265–81
[5] Sun S W and O'Handley R C 1991 *Phys. Rev. Lett.* **66** 2798–801
[6] Szymczak H and Żuberek R 1993 *Acta Phys. Pol.* A **83** 651–9
[7] Szymcak H 1994 *IEEE Trans. Magn.* **30** 702–7
[8] Kim Y K and Silva T J 1996 *Appl. Phys. Lett.* **68** 2885–6
[9] Koch R, Weber M and Rieder K H 1996 *J. Magn. Magn. Mater.* **159** L11–16
[10] Sander D, Enders A and Kirschner J 1999 *J. Magn. Magn. Mater.* **197** at press
[11] Kittel C 1949 *Rev. Mod. Phys.* **21** 541–83
[12] Wu R, Chen L and Freeman A J 1997 *J. Magn. Magn. Mater.* **170** 103–9
[13] Hjortstam O, Baberschke K, Wills J M, Johansson B and Eriksson O 1997 *Phys. Rev.* B **55** 15 026–32
[14] Guo G Y 1997 *J. Magn. Magn. Mater.* **176** 97–110
[15] Moruzzi V L and Marcus P M and Kübler J 1989 *Phys. Rev.* B **39** 6957–61
[16] Wassermann E F 1990 *Invar: Moment-Volume Instabilities in Transition Metals and Alloys (Ferromagnetic Materials 5)* (Amsterdam: Elsevier)
[17] Acet M, Zähres H and Wassermann E F 1994 *Phys. Rev.* B **49** 6012–17
[18] Clark A E and Belson H S 1972 *Phys. Rev.* B **5** 3642–4
[19] Quandt E and Seemann K 1995 *Sensors and Actuators* A **50** 105–9
[20] Quandt E 1997 *J. Alloys Compounds* **258** 126–32
[21] Ibach H 1997 *Surf. Sci. Rep.* **29** 193–264
[22] Jona F and Marcus P M 1994 *Crit. Rev. Surf. Chem.* **4** 189–266
[23] Marcus P M and Jona F 1994 *J. Phys. Chem. Solids* **55** 1513–19
[24] Marcus P M and Jona F 1994 *Surf. Rev. Lett.* **1** 15–21
[25] Marcus P M and Jona F 1995 *Phys. Rev.* B **51** 5263–8
[26] Jona F and Marcus P M 1997 *Surf. Rev. Lett.* **4** 817–20

[27] Matthews J W and Blakeslee A E 1974 *J. Cryst. Growth* **27** 118–25
[28] Matthews J W and Blakeslee A E 1975 *J. Cryst. Growth* **29** 273–80
[29] Matthews J W and Blakeslee A E 1976 *J. Cryst. Growth* **32** 265–73
[30] van der Merwe J H 1979 *The Role of Lattice Misfit in Epitaxy (Chemistry and Physics of Solid Surfaces II)* pp 129–51 (Boca Raton, FL: Chemical Rubber Company)
[31] van der Merwe J H 1982 *Phil. Mag.* A **45** 127–43
[32] van der Merwe J H 1982 *Phil. Mag.* A **45** 145–57
[33] van der Merwe J H 1982 *Phil. Mag.* A **45** 159–70
[34] Markov I V 1995 *Crystal Growth for Beginners: Fundamentals of Nucleation, Crystal Growth, and Epitaxy* (Singapore: World Scientific)
[35] King D A and Woodruff D P (ed) 1997 *Growth and Properties of Ultrathin Epitaxial Layers (The Chemical Physics of Solid Surfaces 8)* (Amsterdam: Elsevier)
[36] Falicov L M *et al* 1990 *J. Mater. Res.* **5** 1299–340
[37] Gradmann U 1993 *Magnetism in Ultrathin Transition Metal Films (Handbook of Magnetic Materials 7)* (Amsterdam: Elsevier) ch 1, pp 1–96
[38] Allenspach R 1994 *J. Magn. Magn. Mater.* **129** 160–85
[39] Bland J A C and Heinrich B (ed) 1994 *Ultrathin Magnetic Structures* vol I (Berlin: Springer)
[40] Bland J A C and Heinrich B (ed) 1994 *Ultrathin Magnetic Structures* vol II (Berlin: Springer)
[41] Ebert H 1996 *Rep. Prog. Phys.* **59** 1665–735
[42] Besenbacher F 1996 *Rep. Prog. Phys.* **59** 1737–802
[43] Farle M 1998 *Rep. Prog. Phys.* **61** 755–826
[44] Lee C H, He H H, Lamelas F J, Vavra W, Uher C and Clarke R 1990 *Phys. Rev.* B **42** 1066–9
[45] Engel B N, England C D, van Leeuwen R A and Wiedmann M H 1991 *J. Appl. Phys.* **70** 5873–5
[46] Chang C R 1993 *Phys. Rev.* B **48** 15 817–22
[47] Yamaguchi A, Ogu S, Soe W H and Yamamoto R 1993 *Appl. Phys. Lett.* **62** 1020–2
[48] Hillebrands B and Dutcher J R 1993 *Phys. Rev.* B **47** 6126–9
[49] Bochi G, Song O and O'Handley R C 1994 *Phys. Rev.* B **50** 2043–6
[50] Krams P and Hillebrands B and Güntherodt G and Oepen H P 1994 *Phys. Rev.* B **49** 3633–6
[51] Schulz B and Baberschke K 1994 *Phys. Rev.* B **50** 13 467–71
[52] Fritzsche H, Kohlhepp J and Gradmann U 1995 *Phys. Rev.* B **51** 15 933–41
[53] Bochi G, Ballentine C A, Inglefield H E, Thompson C V and O'Handley R C 1996 *Phys. Rev.* B **53** R1729–32
[54] Callegaro L and Puppin E 1996 *Appl. Phys. Lett.* **68** 1279–81
[55] Braun A, Feldmann B and Wuttig M 1997 *J. Magn. Magn. Mater.* **171** 16–28
[56] Fassbender J, Güntherodt G, Mathieu C, Hillebrands B, Roberts D J and Gehring G A 1998 *Phys. Rev.* B **57** 5870–8
[57] Ashcroft N W and Mermin N D 1987 *Solid State Physics* (New York: Holt, Rinehart and Winston)
[58] Nye J F 1985 *Physical Properties of Crystals* (Oxford: Oxford University Press)
[59] Landau L D and Lifshitz E M 1970 *Theory of Elasticity* (Oxford: Pergamon)
[60] Hearmon R F S 1969 *The Elastic Constants of Non-Piezoelectric Crystals (Landolt–Börnstein Numerical Data and Functional Relationships in Science and Technology Group III)* vol 2 (Berlin: Springer)
[61] Hearmon R F S 1984 *The Elastic Constants of Crystals and Other Anisotropic Materials (Landolt–Börnstein Numerical Data and Functional Relationships in Science and Technology Group III)* vol 18 (Berlin: Springer)
[62] Donnay J D H and Ondik H M (ed) 1973 *Crystal Data* (Gaithersburg, MD: National Bureau of Standards)
[63] Stearns M B 1986 *Magnetic Properties of 3d, 4d and 5d Elements, Alloys and Compounds (Landolt–Börnstein Numerical Data and Functional Relationships in Science and Technology Group III* vol 19a (Berlin: Springer)
[64] Wulfhekel W 1998 Private communication
[65] Sander D, Schmidthals C, Enders A and Kirschner J 1998 *Phys. Rev.* B **57** 1406–9
[66] Kämper K P, Schmitt W, Güntherodt G and Kuhlenbeck H 1988 *Phys. Rev.* B **38** 9451–6
[67] Kämper K P, Schmitt W, Wesner D A and Güntherodt G 1989 *Appl. Phys.* A **49** 573–8
[68] Koziol C, Lilienkamp G and Bauer E 1990 *Phys. Rev.* B **41** 3364–71
[69] Harrison W A 1980 *Solid State Theory* (New York: Dover)
[70] Sutton A P 1994 *Electronic Structure of Materials* (Oxford: Clarendon)
[71] Hübner W 1998 Private communication
[72] Zangwill A 1988 *Physics at Surfaces* (Cambridge: Cambridge University Press)
[73] Desjonquères M C and Spanjaard D 1996 *Concepts in Surface Physics* (Berlin: Springer)
[74] Brantley W A 1973 *J. Appl. Phys.* **44** 534–5

[75] Clark A E 1980 *Magnetostrictive Rare Earth-Fe_2 Compounds (Ferromagnetic Materials 1)* (Amsterdam: North-Holland)
[76] Becker R and Döring W 1939 *Ferromagnetismus* (Berlin: Springer)
[77] Carr W J Jr 1966 *Secondary Effects in Ferromagnetism (Handbuch der Physik XVIII/2)* (Berlin: Springer)
[78] Shick A B, Novikov D L and Freeman A J 1997 *Phys. Rev.* B **56** R14 259–62
[79] Mason W P 1951 *Phys. Rev.* **82** 715–23
[80] Mason W P 1954 *Phys. Rev.* **96** 302–10
[81] Döring W and Simon W 1960 *Ann. Phys.* **5** 373–87
[82] du Trémolet de Lacheisserie E 1993 *Magnetostriction* (Boca Raton, FL: Chemical Rubber Company)
[83] Bruno P 1993 *Magnetismus von Festkörpern und Grenzflächen (Physical Origins and Theoretical Models of Magnetic Anisotropy* (Jülich: Forschungszentrum Jülich) pp 24.1–24.28
[84] Carr W J and Smoluchowski R 1951 *Phys. Rev.* **83** 1236–43
[85] Bozorth R M and Hamming R W 1953 *Phys. Rev.* **89** 865–9
[86] Lee E W and Asgar M A 1971 *Proc. R. Soc.* A **326** 73–85
[87] Bower D I 1971 *Proc. R. Soc.* A **326** 87–96
[88] Bozorth R M 1954 *Phys. Rev.* **96** 311–16
[89] Hubert A, Unger W and Kranz J 1969 *Z. Phys.* **224** 148–55
[90] Bruno P 1988 *J. Phys. F: Met. Phys.* **18** 1291–8
[91] Fujiwara H, Kadomatsu H and Tokunaga T 1983 *J. Magn. Magn. Mater.* **31–34** 809–10
[92] Takahashi H, Tsunashima S, Iwata S and Uchiyama S 1993 *J. Magn. Magn. Mater.* **126** 282–4
[93] du Trémolet de Lacheisserie E 1995 *Phys. Rev.* B **51** 15 925–32
[94] Néel L 1954 *J. Phys. Rad.* **15** 225–39
[95] Trémolet de Lacheisserie and McGrath O F K 1995 *J. Magn. Magn. Mater.* **147** 160–6
[96] White R L and Clemens B M 1992 *Mat. Res. Soc. Symp.* **231** 453–8
[97] Kim M, Zhong L and Freeman A J 1998 *Phys. Rev.* B **57** 5271–5
[98] Kyuno K, Ha J-G, Yamamoto R and Asano S 1996 *Phys. Rev.* B **54** 1092–9
[99] Song O, Ballentine C A and O'Handley R C 1994 *Appl. Phys. Lett.* **64** 2593–5
[100] O'Handley R C and Sun S W 1992 *J. Magn. Magn. Mater.* **104–107** 1717–20
[101] O'Handley R C and Sun S 1992 *Mat. Res. Soc. Symp. Proc.* **231** 485–90
[102] O'Handley R C, Oh-Sung Song and Ballentine C A 1993 *J. Appl. Phys.* **74** 6302–7
[103] Barandiarán J M, Hernando A, Madurga V, Nielsen O V, Vázquez M and Vázquez-López M 1987 *Phys. Rev.* B **35** 5066–71
[104] Siemko A and Lachowicz H K 1987 *J. Magn. Magn. Mater.* **66** 31–6
[105] Tsunashima S, Nakamura K and Uchiyama S 1990 *IEEE Trans. Magn.* **26** 2724–6
[106] Nakamura K, Tsunashima S and Uchiyama S 1991 *J. Magn. Magn. Mater.* **93** 462–4
[107] Takahashi H, Fukatsu S, Tsunashima S and Uchiyama S 1992 *J. Magn. Magn. Mater.* **104–107** 1831–2
[108] Takahashi H, Tsunashima S, Iwata S and Uchiyama S 1993 *Japan. J. Appl. Phys.* **32** L1328–31
[109] Wu R and Freeman A J 1996 *J. Appl. Phys.* **79** 6209–12
[110] Söderlind P, Ahuja R, Eriksson O, Wills J M and Johansson B 1994 *Phys. Rev.* B **50** 5918–27
[111] Gay J G and Richter R 1986 *Phys. Rev. Lett.* **56** 2728–31
[112] Daalderop G H, Kelly P J and den Broeder F J A 1992 *Phys. Rev. Lett.* **68** 682–5
[113] Wang D S, Wu R and Freeman A J 1993 *Phys. Rev. Lett.* **70** 869–72
[114] Wang D S, Wu R and Freeman A J 1993 *Phys. Rev.* B **47** 14 932–47
[115] Wang D S, Wu R and Freeman A J 1994 *J. Magn. Magn. Mater.* **129** 237–58
[116] Victora R H and MacLaren J M 1993 *Phys. Rev.* B **47** 11 583–6
[117] Wang D S, Wu R and Freeman A J 1993 *J. Appl. Phys.* **73** 6745–7
[118] Lachowicz H K and Szymczak H 1984 *J. Magn. Magn. Mater.* **41** 327–34
[119] Clark A E, DeSavage B F and Bozorth R 1963 *Phys. Rev.* **138** A216–24
[120] Hoekstra B, Gyorgy E M, Zydzik G and Flanders P J 1977 *Rev. Sci. Instrum.* **48** 1253–5
[121] Callen E R, Clark A E, DeSavage B and Coleman W 1963 *Phys. Rev.* **130** 1735–40
[122] Fawcett E 1970 *Phys. Rev.* B **2** 1604–13
[123] Tsuya N, Arai K I, Shiraga Y, Yamada M and Masumoto T 1975 *Phys. Status Solidi* A **31** 557–61
[124] Giallorenzi T G, Bucaro J A, Dandridge A, Sigel J R G H, Cole J H and Rasleigh S C 1982 *IEEE J. Quantum Electron.* **QE-18** 626–65
[125] Bucholtz F, Koo K P, Sigel G H Jr and Dandridge A 1985 *IEEE J. Lightwave Tech.* **LT-3** 814–17
[126] Squire P T and Gibbs M R 1987 *J. Phys. E: Sci. Instrum.* **20** 499–502
[127] Gates L and Stroink G 1992 *Rev. Sci. Instrum.* **63** 2017–20
[128] Brizzolara R A and Colton R J 1990 *J. Magn. Magn. Mater.* **88** 343–50

[129] Costa J L, Nogués J and Rao K V 1994 *J. Appl. Phys.* **76** 7030
[130] Pidgeon H A 1919 *Phys. Rev.* **13** 209–37
[131] Liniers M, Madurga V, Vázquez M and Hernando A 1985 *Phys. Rev.* B **31** 4425–32
[132] Drosdziok S and Wessel K 1973 *IEEE Trans. Magn.* **MAG-9** 56–9
[133] Vázquez M, Fernengel W and Kronmüller H 1983 *Phys. Status Solidi* A **80** 195–204
[134] Hernando A and Prados C 1994 *Elektrotechn. Čas* **45** 126–9
[135] Huang J, Prados C, Evetts J E and Hernando A 1995 *Phys. Rev.* B **51** 297–304
[136] Callegaro L, Puppin E and Petrali D 1997 *Rev. Sci. Instrum.* **68** 1796–9
[137] Hilzinger H R, Hillmann H and Mager A 1979 *Phys. Status Solidi* A **55** 763–9
[138] Mitra A and Vázquez M 1990 *J. Appl. Phys.* **67** 4986–8
[139] Yamasaki J, Ohkubo Y and Humphrey F B 1990 *J. Appl. Phys.* **67** 5472–4
[140] Gomez-Polo C, Pulido E, Rivero G Hernando A 1990 *J. Appl. Phys.* **67** 4984–5
[141] Wenda J, Jankowski H and Kulak A 1987 *Thin Solid Films* **148** 1–6
[142] Huang J, Arnott M G, Somekh R E and Evetts J E 1993 *IEEE Trans. Magn.* **29** 3093–5
[143] Eastman D E 1967 *Phys. Rev.* **156** 645–54
[144] Smith A B 1967 *Rev. Sci. Instrum.* **39** 378–85
[145] Bushnell S E, Nowak W B, Oliver S A and Vittoria C 1992 *Rev. Sci. Instrum.* **63** 2021–5
[146] McMichael R D 1994 *J. Appl. Phys.* **75** 5650–2
[147] Cochran J F 1994 *Light Scattering from Ultrathin Magnetic Layers and Bilayers (Ultrathin Magnetic Structures II)* (Berlin: Springer)
[148] Hillebrands B and Güntherodt G 1994 *Brillouin Light Scattering in Magnetic Superlattices (Ultrathin Magnetic Structures II)* (Berlin: Springer)
[149] Schell-Sorokin A J and Tromp R M 1990 *Phys. Rev. Lett.* **64** 1039–42
[150] Schell-Sorokin A J and Tromp R M 1994 *Surf. Sci.* **319** 110–18
[151] Sander D, Skomski R, Schmidthals C, Enders A and Kirschner J 1996 *Phys. Rev. Lett.* **77** 2566–9
[152] Koch R 1997 *Intrinsic Stress of Epitaxial Thin Films and Surface Layers (The Chemical Physics of Solid Surfaces 8)* (Amsterdam: Elsevier)
[153] Sander D, Enders A and Kirschner J 1995 *Appl. Phys. Lett.* **67** 1833–5
[154] Volkert C A 1991 *J. Appl. Phys.* **70** 3521–7
[155] Klokholm E 1976 *IEEE Trans. Magn.* **MAG-12** 819–21
[156] Tam A C and Schroeder H 1988 *J. Appl. Phys.* **64** 5422–4
[157] Tam A C and Schroeder H 1989 *IEEE Trans. Magn.* **25** 2629–38
[158] du Trémolet de Lacheisserie E and Peuzin J C 1994 *J. Magn. Magn. Mater.* **136** 189–96
[159] Betz J, du Trémolet de Lacheisserie E and Baczewski L T 1996 *Appl. Phys. Lett.* **68** 132–3
[160] Osiander R, Ecelberger S A, Gvens R B, Wickende D K, Murphy J C and Kistenmacher T J 1996 *Appl. Phys. Lett.* **96** 2930–1
[161] Doerner M F and Nix W D 1988 *CRC Crit. Rev. Solid State Mater. Sci.* **14** 225–67
[162] Abermann R 1990 *Vacuum* **41** 1279–82
[163] Koch R 1994 *J. Phys.: Condens. Matter* **6** 9519–50
[164] Hoffman R W 1966 *Phys. Thin Films* **3** 211–73
[165] Kinosita K 1972 *Thin Solid Films* **12** 17–28
[166] Nix W D 1989 *Metall. Trans.* A **20** 2217–45
[167] Weihs T P, Hong S, Bravman J C and Nix W D 1988 *J. Mater. Res.* **3** 931–42
[168] Flinn D A, Gardner D S and Nix W D 1987 *IEEE Trans. Electron. Dev.* **ED-34** 689–99
[169] Geisz J F, Kuech T F, Lagally M G, Cardone F and Potemski R M 1994 *J. Appl. Phys.* **75** 1530–3
[170] Ruud J A, Witvrouw A and Spaepen F 1993 *J. Appl. Phys.* **74** 2517–23
[171] Floro J A, Chason E, Lee S R, Twesten R D, Hwang R Q and Freund L B 1997 *J. Electron. Mater.* **26** 969–79
[172] Martinez R A, Augustyniak W M and Golovchenko J A 1990 *Phys. Rev. Lett.* **64** 1035–8
[173] Sander D and Ibach H 1991 *Phys. Rev.* B **43** 4263–7
[174] Ibach H 1994 *J. Vac. Sci. Technol.* A **12** 2240–5
[175] Grossmann A, Erley W and Ibach H 1994 *Surf. Sci.* **313** 209–14
[176] Grossmann A, Erley W and Ibach H 1995 *Surf. Rev. Lett.* **2** 543–8
[177] Grossmann A and Erley W, Hannon J B and Ibach H 1996 *Phys. Rev. Lett.* **77** 127–30
[178] Ibach H and Grossmann A 1997 *Mat. Res. Soc. Symp. Proc.* **440** 15–24
[179] Sander D, Enders A and Kirschner J 1999 *Europhys. Lett.* **45** 208–14
[180] Haiss W, Nichols R J and Sass J K 1997 *Surf. Sci.* **388** 141–9
[181] Sander D, Linke U and Ibach H 1992 *Surf. Sci.* **272** 318–25
[182] Bach C E, Giesen M, Ibach H and Einstein T L 1997 *Phys. Rev. Lett.* **78** 4225–8

[183] Ibach H, Bach C E, Giesen M and Grossmann A 1997 *Surf. Sci.* **375** 107–19
[184] Weber M, Koch R and Rieder K H 1994 *Phys. Rev. Lett.* **73** 1166–9
[185] Koch R, Weber M, Henze E and Rieder K H 1995 *Surf. Sci.* **331–333** 1398–403
[186] Sander D, Skomski R, Enders A, Schmidthals C, Reuter D and Kirschner J 1998 *J. Phys. D: Appl. Phys.* **31** 663–70
[187] Sander D, Enders A and Kirschner J 1998 *IEEE Trans. Magn.* **34** 2015–17
[188] Cowburn R P, Moulin A M and Welland M E 1997 *Appl. Phys. Lett.* **71** 2202–4
[189] Rossel C, Willemin M, Gasser A, Bothuizen H, Meijer G I and Keller H 1998 *Rev. Sci. Instrum.* **69** 3199–203
[190] Bader S D 1991 *J. Magn. Magn. Mater.* **100** 440–54
[191] Bader S D and Erskine J L 1994 *Magneto-Optical Effects in Ultrathin Films (Ultrathin Magnetic Structures II)* (Berlin: Springer) ch 4, pp 297–325
[192] Itoh A, Uekusa H, Tarusawa Y, Inoue F and Kawanishi K 1983 *J. Magn. Magn. Mater.* **35** 241–2
[193] Awano H, Suzuki Y, Katayama T and Itoh A 1990 *IEEE Trans. Magn.* **26** 2742–4
[194] Enders A, Sander D and Kirschner J 1999 *J. Appl. Phys.* **85**
[195] Marcus P M 1996 *Surf. Sci.* **366** 219–27
[196] Fukuda T 1995 *Japan. J. Appl. Phys.* **34** 3209–15
[197] Fukuda T 1996 *Japan. J. Appl. Phys.* **35** 3799–806
[198] Timoshenko S and Woinowsky-Krieger S 1959 *Theory of Plates and Shells* (Singapore: McGraw-Hill)
[199] Röll K 1976 *J. Appl. Phys.* **47** 3224–9
[200] Brenner A and Senderoff S 1949 *J. Res. NBS* **42** 105–23
[201] von Preissig F J 1989 *J. Appl. Phys.* **66** 4262–8
[202] Stoney G G 1909 *Proc. R. Soc.* A **82** 172–5
[203] Watts R, Gibbs M R J, Karl W J and Szymczak H 1997 *Appl. Phys. Lett.* **70** 2607–9
[204] van de Ried E 1994 *J. Appl. Phys.* **76** 584–6
[205] Klokholm E and Jahnes C V 1996 *J. Magn. Magn. Mater.* **152** 226–30
[206] du Trémolet de Lacheisserie E and Peuzin J C 1996 *J. Magn. Magn. Mater.* **152** 231–2
[207] Marcus P M 1996 *Phys. Rev.* B **53** 2481–6
[208] Marcus P M 1996 *Phys. Rev.* B **54** 3662
[209] Marcus P M 1997 *J. Magn. Magn. Mater.* **168** 18–24
[210] Hernando A, Neuweiler A, Farber P and Kronmüller H 1998 *Phys. Rev.* B **57** 7458–61
[211] Sander D, Enders A and Kirschner J 1995 *Rev. Sci. Instrum.* **66** 4734–5
[212] Meyer G and Amer N 1988 *Appl. Phys. Lett.* **53** 1045–7
[213] Alexander S, Hellemans L, Marti O, Schneir J, Elings V, Hansma P K, Longmire M and Gurley J 1989 *J. Appl. Phys.* **65** 164–7
[214] Meyer G and Amer N M 1990 *Appl. Phys. Lett.* **56** 2100–1
[215] Enders A 1999 Mechanische Spannungen und Ferromagnetismus ultradünner Schichten *PhD Thesis* Martin-Luther Universität Halle-Wittenberg, Mathematisch-Naturwissenschaftlich-Technische Fakultät
[216] Gradmann U, Korecki J and Waller G 1986 *Appl. Phys.* A **39** 101–8
[217] Elmers H J, Hauschild J, Fritzsche H, Liu G, Gradmann U and Köhler U 1995 *Phys. Rev. Lett.* **75** 2031–4
[218] Weber N, Wagner K, Elmers H J, Hauschild J and Gradmann U 1997 *Phys. Rev.* B **55** 14 121–4
[219] Hauschild J, Gradmann U and Elmers H J 1998 *Appl. Phys. Lett.* **72** 3211–13
[220] Sander D, Enders A, Skomski R and Kirschner J 1996 *IEEE Trans. Magn.* **32** 4570–2
[221] Gradmann U and Waller G 1982 *Surf. Sci.* **116** 539–48
[222] Albrecht M, Gradmann U, Reinert Th and Fritsche L 1991 *Solid State Commun.* **78** 671–5
[223] Tober E D, Ynzunza R X, Palomares F J, Wang Z, Hussain Z, van Hove M A and Fadley C S 1997 *Phys. Rev. Lett.* **79** 2085–8
[224] Sander D, Enders A, Schmidthals C, Reuter D and Kirschner J 1998 *Surf. Sci.* **402–404** 351–5
[225] Batirev I G, Hergert W, Rennert P, Stepanyuk V S, Oguchi T, Katsnelson A A, Leiro J A and Lee K H 1998 *Surf. Sci.* **417** 151–8
[226] Bethge H, Heuer D, Jensen Ch, Reshöft K and Köhler U 1995 *Surf. Sci.* **331–333** 878–84
[227] Jensen C, Reshöft K and Köhler U 1996 *Appl. Phys.* A **62** 217–21
[228] Bode M, Pascal R, Dreyer M and Wiesendanger R 1996 *Phys. Rev.* B **54** R8385–8
[229] Elmers H J and Gradmann U 1990 *Appl. Phys.* A **51** 255–63
[230] Bruno P 1988 *J. Appl. Phys.* **64** 3153–6
[231] Chappert C and Bruno P 1988 *J. Appl. Phys.* **64** 5736–41
[232] Bruno P and Renard J-P 1989 *Appl. Phys.* A **49** 1833–5
[233] Reuter D, Gerth G and Kirschner J 1997 Surface diffusion of 3d-metals on W(110) *Surface Diffusion: Atomistic and Collective Processes* (New York: Plenum) pp 489–98

[234] Reuter D, Gerth G and Kirschner J 1998 *Phys. Rev.* B **57** 2520–9
[235] Skomski R and Coey J M D 1993 *Phys. Rev.* B **48** 15 812–16
[236] Gradmann U, Liu G, Elmers H J and Przybylski M 1990 *Hyperfine Interact.* **57** 1845–58
[237] Berlowitz P J, He J W and Goodman D W 1990 *Surf. Sci.* **231** 315–24
[238] Sander D, Enders A, Schmidthals C, Reuter D and Kirschner J 1998 *J. Magn. Magn. Mater.* **177–181** 1299–300
[239] Prinz G A, Rado G T and Krebs J J 1982 *J. Appl. Phys.* **53** 2087–91
[240] Lu L, Bansmann J and Meiwes-Broer K H 1998 *J. Phys.: Condens. Matter* **10** 2873–80
[241] Przybylski M, Kaufmann I and Gradmann U 1989 *Phys. Rev.* B **40** 8631–40
[242] Fink R L, Mulhollan G A, Andrews A B, Erskine J L and Walters G K 1991 *J. Appl. Phys.* **69** 4986–8
[243] Chen J and Erskine J L 1992 *Phys. Rev. Lett.* **68** 1212–15
[244] Elmers H J and Hauschild J 1994 *Surf. Sci.* **320** 134–44
[245] Matthews J W and Crawford J L 1970 *Thin Solid Films* **5** 187–98